remote sensing

MDPI

Article

Distinguishing Lithofacies of Flysch Formations Using Deep Learning Models: Integrating Remote Sensing Data with Morphological Indexes

Paraskevas Tsangaratos [1,*], Ioannis Vakalas [1,2] and Irene Zanarini [3]

[1] Department of Geological Sciences, School of Mining and Metallurgical Engineering, National Technical University of Athens, Iroon Polytechniou 9 Str., Zografou Campus, 15773 Athens, Greece; ivakalas@metal.ntua.gr
[2] Institute of GeoEnergy, Technical University of Crete Campus, 73100 Chania, Greece
[3] Hellenic Survey of Geology & Mineral Exploration (HSGME), 1 Spirou Loui Str., 13677 Acharnae, Greece; izananiri@eagme.gr
* Correspondence: ptsag@metal.ntua.gr

Abstract: The main objective of the present study was to develop an integrated approach combining remote sensing techniques and U-Net-based deep learning models for lithology mapping. The methodology incorporates Landsat 8 imagery, ALOS PALSAR data, and field surveys, complemented by derived products such as False Color Composites (FCCs), Minimum Noise Fraction (MNF), and Principal Component Analysis (PCA). The Dissection Index, a morphological index, was calculated to characterize the geomorphological variability of the region. Three variations of the deep learning U-Net architecture, Dense U-Net, Residual U-Net, and Attention U-Net, were implemented to evaluate the performance in lithological classification. Validation was conducted using metrics such as the accuracy, precision, recall, F1-score, and mean intersection over union (mIoU). The results highlight the effectiveness of the Attention U-Net model, which provided the highest mapping accuracy and superior feature extraction for delineating flysch formations and associated lithological units. This study demonstrates the potential of integrating remote sensing data with advanced machine learning models to enhance geological mapping in challenging terrains.

Keywords: lithology mapping; deep learning; U-Net models; flysch formations

check for updates

Academic Editors: Xiaobo Liu, Yaoming Cai and Pedram Ghamisi

Received: 14 December 2024
Revised: 23 January 2025
Accepted: 24 January 2025
Published: 26 January 2025

Citation: Tsangaratos, P.; Vakalas, I.; Zanarini, I. Distinguishing Lithofacies of Flysch Formations Using Deep Learning Models: Integrating Remote Sensing Data with Morphological Indexes. *Remote Sens.* **2025**, *17*, 422. https://doi.org/10.3390/rs17030422

Copyright: © 2025 by the authors. Licensee MDPI, Basel, Switzerland. This article is an open access article distributed under the terms and conditions of the Creative Commons Attribution (CC BY) license (https://creativecommons.org/licenses/by/4.0/).

1. Introduction

Lithological mapping is a fundamental process in geology that involves the systematic study and representation of the distribution and characteristics of geological formations on the Earth's surface [1,2]. It plays a crucial role in understanding geological history, identifying natural resources, assessing geological hazards, and supporting various geoscientific applications [3]. Advancements in satellite remote sensing have revolutionized lithological mapping, providing cost-effective alternatives to traditional fieldwork, particularly in remote or hard-to-access regions [4,5]. Remote sensing leverages the distinct spectral signatures of rocks, which uniquely reflect electromagnetic energy across various wavelengths. This spectral variability forms the foundation of automated lithological classification methods, enabling the identification of rocks' mineralogical characteristics with precision [4]. As pointed out by Dong et al. [6], the advancement of remote sensing technology has introduced an efficient and convenient approach to geological work. No-

tably, remote sensing lithological classification stands out for its rapid processing, robust macroscopic observation capabilities, and overall efficiency.

In recent years, the application of machine learning has enhanced the efficiency, accuracy, and scope of geological studies and has transformed lithological mapping by enabling automated pattern extraction from large datasets using statistical and heuristic approaches [2,7,8]. In terms of the methodological processes, two main categories can be distinguished [4,9,10]: (i) methods that follow unsupervised classification processes, in which spectral data are grouped without the need for training bands, and (ii) methods that follow supervised classification processes, in which pixels are assigned to predefined classes based on labeled training data. In lithology mapping, supervised classification techniques such as maximum likelihood classifier (MLC), naive Bayes (NB), artificial neural networks (ANNs), k-nearest neighbors (K-NNs), random forest (RF), and support vector machines (SVMs) are widely adopted methods [8,10,11]. Advance machine learning models such as hybrid attention-integrated Long Short-Term Model networks, leveraging multi-source data fusion and advanced attention mechanisms, have demonstrated significant advancements in remote sensing tasks, particularly in lithological unit identification, by addressing challenges such as class imbalance and interclass similarities while improving the classification accuracy [12]. Additionally, high-resolution geospatial analysis combined with remote sensing techniques has proven instrumental in characterizing hydrogeological systems, such as karstic formations, by integrating morpho-structural information to enhance our understanding of water infiltration and pollution vulnerability [13]. El-Omairi et al. [10] highlight that combining remote sensing with machine learning algorithms provides an effective method for classifying various lithological units. This approach proves especially valuable in regions that are difficult to access, underlining its significance in geological studies and environmental management.

While traditional machine learning models have proven effective, their reliance on manually extracted features can limit the accuracy in complex geological scenarios. Deep learning, a subset of machine learning, overcomes this limitation by automatically learning hierarchical features directly from raw data, thereby eliminating the need for manual feature engineering [14–17]. Convolutional neural networks (CNNs), popular deep learning architectures, have achieved remarkable success in remote sensing tasks, including lithological mapping, by capturing both spatial and contextual information at multiple scales [18–20]. Among deep learning models, U-Net and its advanced variants have emerged as powerful tools for pixel-level classification [21]. These architectures are particularly adept at processing geospatial data by preserving spatial resolution and extracting fine-grained features, enabling the precise delineation of lithological boundaries and the differentiation of closely related rock units [22,23].

Notable studies concerning the application of U-Net model are the ones presented by Liu et al. [22], who utilized U-Net-based segmentation for ore particle images for tasks related to mineral identification and particle analysis. The study by Liu et al. [24] reported the successful implementation of a Transformer + UNet hybrid model, which achieved a 95.57% accuracy in lithology identification, and an optimized ResNet-18 model, which reached 96.13% accuracy in assessing rock weathering degrees. The study by Pollat et al. [25] developed an automated U-Net-based DenseNet121 method using transfer learning to detect dolines, hazardous karstic depressions, near Sivas City, Turkey. The study of Chen et al. 2024 [26] applied Mobilenet-based U-Net, Mobilenet-based PSPNet, and SegNet for the semantic segmentation of remote sensing images to improve geological mapping tasks such as lithological and soil type classification.

From the review of the available studies concerning the application of U-Net models and their variants, the transformative potential of deep learning for accurate lithological

mapping and geological segmentation is evident. In most cases, these models excel in extracting spatial and contextual features from raw data, delivering high accuracy and reliability in geological studies. However, their performance depends heavily on the quality and diversity of input data. While single-source datasets, such as spectral imagery from sensors like Landsat 8, are effective in specific cases, integrating multi-source data offers notable advantages. As demonstrated by Wang et al. [15], the fusion of geochemical, geophysical, and remote sensing data enables holistic analyses, improving the accuracy and robustness of predictive models for geological mapping. Mahmood et al. [2] utilized Landsat 5 TM imagery to map lithology in the forested, inaccessible montane terrain of the Chittagong Hill Tracts, Bangladesh. Using vegetation and drainage patterns as proxies for underlying rock types, supervised and unsupervised classification methods, combined with field observations, provide a more spatially detailed map of sandstone and shale distributions. Similarly, studies like Bachri et al. [4] and Ghoneim et al. [27] show that combining spectral features with geomorphometric attributes or field data enhances lithological discrimination and mapping precision. In more detail, Bachri et al. [4] integrated Landsat 8 OLI spectral data with DEM-derived geomorphometric variables (slope, curvature, and surface roughness) to enhance lithological mapping in the Souk Arbaa Sahel region, Southern Morocco. Using an SVM model, they achieved an 85% overall accuracy and concluded that combining geomorphological and spectral data significantly improved the detail and accuracy of lithological mapping. Similarly, Le et al. [28] demonstrated the effectiveness of integrating DEM-derived geomorphometric variables, such as slope, curvature, and surface roughness, with remote sensing data for improved lithological classification. By utilizing ASTER imagery, ASTER-derived DEM, and aeromagnetic data, they applied the support vector machine (SVM) algorithm to classify lithological units in northwestern India. The study underscores the critical role of DEM-derived features in enhancing lithological discrimination and highlights the utility of the SVM as a robust method for producing accurate first-pass lithological maps in regions with limited prior geological information.

In this context, the main objective of our study was to implement different U-Net-based deep learning models to enhance lithology mapping using multi-source data, including Landsat 8 imagery, ALOS PALSAR data, and field surveys. Specifically, from the Landsat 8 imagery database and applying visualization, statistical, and transformation remote sensing techniques, we expect to extract and enhance significant information. From the ALOS PALSAR data, we applied geospatial analysis to assess geomorphological characteristics, specifically, the Dissection Index that expresses the geomorphological variability, providing a novel dimension for distinguishing lithological units. Combining the above with ground truth data, we utilized three U-Net models, Dense U-Net, Residual U-Net, and Attention U-Net, comparing their performance, and provide valuable conclusions in regard to the performance of all models in different lithological units. This study was conducted in two distinct regions: one with five lithological units and the other with two, enabling a comparative analysis of U-Net-based deep learning models across varying lithological complexities. By applying a consistent methodological framework—integrating Landsat 8, ALOS PALSAR, and field survey data—we evaluated the models' adaptability to differences in geological variability and unit diversity. This approach validated the models' robustness and generalizability while providing valuable insights into their effectiveness in delineating lithological boundaries in both simple and complex terrains.

2. Materials and Methods

2.1. Study Area

The study area (Figure 1) is in Akarnania region in Greece, and it is dominated by flysch deposits. From a structural point of view, flysch deposits are part of the Pindos foreland [29,30], a Tertiary basin trending parallel to the external Hellenides, occupying the Gavrovo and Ionian isopic zones [31]. The basin is bounded to the east by the Pindos thrust and to the west by the Ionian thrust. The Gavrovo thrust separates the Gavrovo and Internal Ionian zones. In addition to these major thrusts, two minor thrusts divide the Ionian zone into the internal, middle, and external Ionian zone (from the east to the west) [32]. The area where the analysis took place (Figure 1, red rectangle) is covered by the geological maps of the Hellenic Survey of Geology and Mineral Exploration sheets "Agrinion" and "Myrofyllon" [33,34]. Tertiary flysch overlies the Mesozoic facies of the Hellenides orogenic belt, deposited on a series of platforms (Pre-Apulian and Gavrovo zones) and deep basins (Ionian and Pindos zones) that formed the eastern rifted margin of the Apulian plate, bordering towards the east Pindos zone [31–33]. Similar basins are the Oligocene to Recent basins of the northern Apennines [34] that continue into the Ionian Sea and are also characterized by internal thrusting. Intrabasinal highs and splitting of the basin into parallel sub-basins is the product of internal thrusting activity [35,36]. These units (external Hellenides), were developed during Tertiary times following the closure of the Pindos ocean and the consequent continent–continent collision between the Apulian and Pelagonia microcontinents to the east, resulting in the inversion of Mesozoic basins, forming a series of thrust sheets [37–39]. Sedimentation and depositional environments in foreland basin settings are mainly controlled by gravity flow deposits. These types of flow favor the deposition of significant volumes of sediment and control submarine fan architecture. The economic significance of such a type of basin fill has been proven by the fact that they host some of the largest oil and gas reserves [40]. In the study area, flysch deposits were first assessed as being submarine fan deposits by Piper et al. [41]. Other researchers supported this approach by studying several exposures of flysch in the area [42–50].

The age of Pindos foreland sediments is still a matter of discussion. B.P. [51] proposed an early Miocene to middle Miocene age, explaining the presence of Oligocene fauna as a product of large-scale erosion and reworking of older sediments during the Miocene. IGSR and IFP [32] suggested a late Eocene to early Miocene age for the basin fill while Fleury [52], Leigh [47], Wilpshaar [53], and Bellas [54] assigned an Oligocene age. Vakalas [40], based on calcareous nannofossils originating from 16 lithostratigraphic sections across the Internal Ionian zone, proposed a Middle Eocene to Late Oligocene age. Avramidis [49] proposed a middle Eocene to early Miocene age, using nannofossil zones from three studied cross-sections in the Klematia-Paramythia basin (middle Ionian zone) [Figure 2]. Geological mapping of submarine fan facies plays a key role in the primary identification of potential reservoir units. The present study aims to assess the usefulness of machine learning techniques in the mapping of mud-dominated and sand-dominated submarine fan facies, using as input high-resolution DEM models and geological maps of the study area.

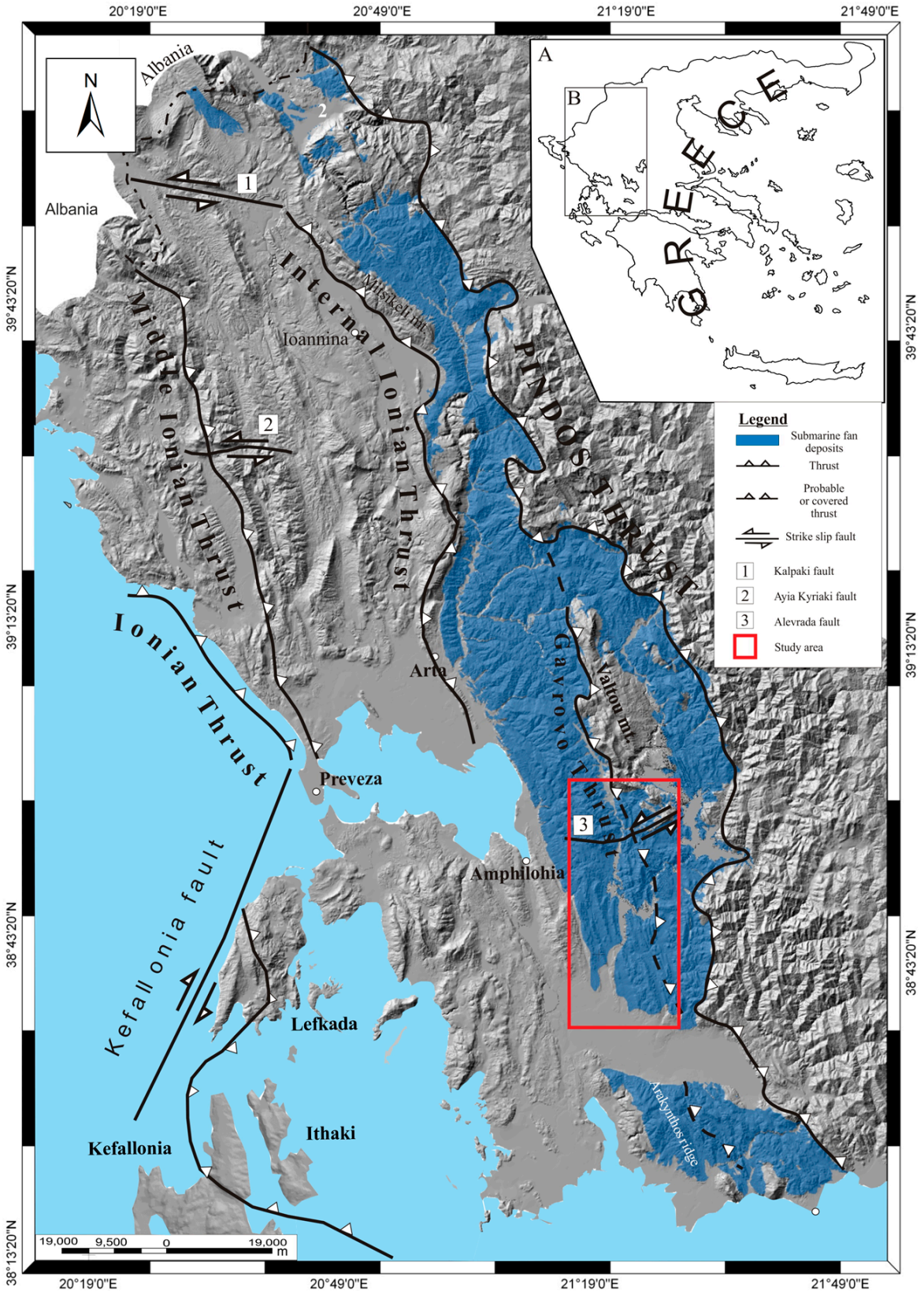


Figure 1. Map showing the study area, with (A) presenting Greece for context and (B) outlining the broader research region. The red rectangle indicates the specific focus area.

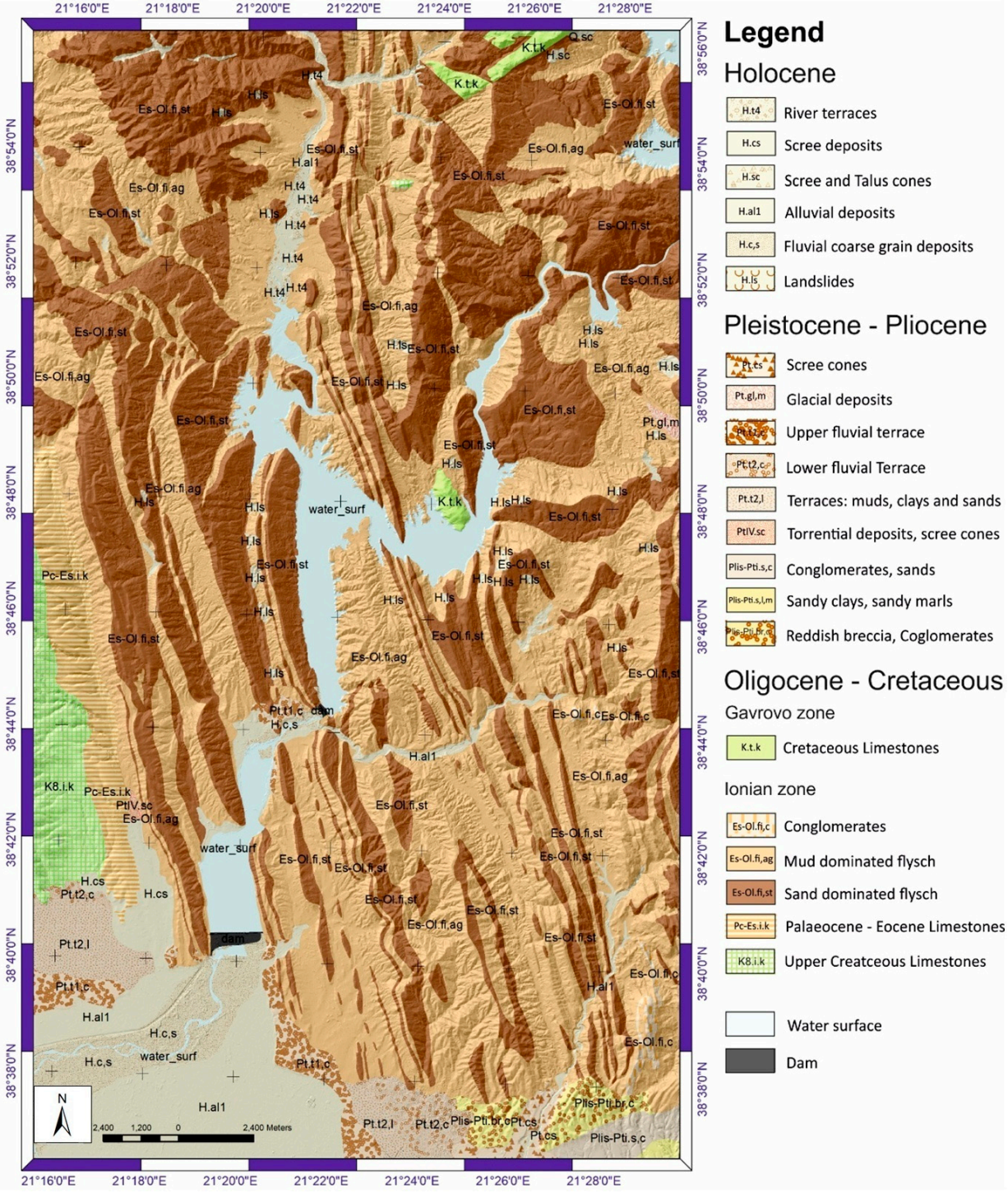


Figure 2. The lithology of the research area. Mud- and sand-dominated flysch facies as shown in the available geological maps [33,34]. Greenish exposures correspond to the Mesozoic basement.

2.2. Methodology

The methodology involves a three-step procedure: data collection and processing, implementation of deep learning models, and modeling and validation. In the first step, three spectral enhancement techniques were utilized, including Color Ratio Composites (CRCs), Principal Component Analysis (PCA), and Minimum Noise Fraction (MNF), while the Dissection Index was derived from a Digital Elevation Model (DEM) to capture topographic features. The workflow involves loading and resizing multiple geospatial raster datasets (DEM, FCC, MNF, and PCA) to match dimensions and stacking them into a 10-band input.

It extracts image patches, maps lithology classes to sequential integers, and trains a model using focal loss and accuracy as performance metrics. After training, the model predicts lithology maps for validation patches and reconstructs predictions for the full area. These processed datasets were used to train advanced deep learning models, such as the Dense U-Net, the Residual U-Net, and the Attention U-Net, which were validated using metrics like accuracy, precision, recall, F1-score, and IoU to ensure accurate and robust lithological mapping. The implementation of the Dense U-Net, Residual U-Net, and Attention U-Net models was conducted on the Kaggle platform, utilizing its cloud-based environment with dual NVIDIA Tesla T4 GPUs (GPU T4 ×2) to facilitate parallel processing for computationally intensive tasks [55]. Python served as the primary programming language, leveraging TensorFlow and Keras libraries, which provided efficient tools for model development, training, and optimization, including support for convolutional layers, batch normalization, and advanced loss functions [56]. Figure 3 illustrates the developed methodology, whereas a brief description of the data and methods follows.

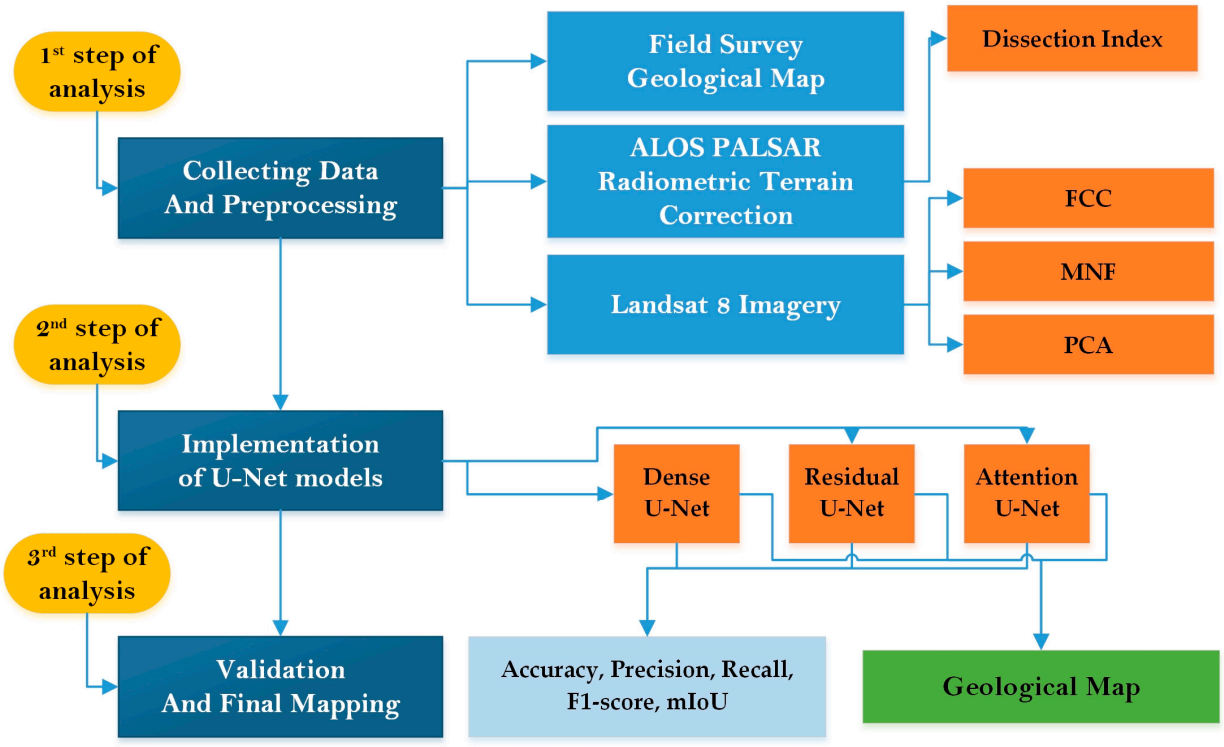


Figure 3. Flowchart of the developed methodology, illustrating the three-step process: data collection and preprocessing, implementation of U-Net models, and validation leading to the final geological map.

2.2.1. Collect and Preprocessing Data

The first step of analysis involved obtaining and processing the remote sensing data, the DEM, and the ground truth data from geological maps and field surveys.

Field Survey—Geological Survey—Ground Truth Data

The "Agrinion" and "Myrofyllon" geological map sheets served as indispensable sources of ground truth data for this study [33,34]. Prepared at a detailed 1:50,000 scale, these maps provided high-resolution insights into the region's geological landscape, enabling precise identification of geological formations, structural features, and land deformation patterns. Their accuracy and detail were particularly valuable in distinguishing

between the mud-dominated and sand-dominated flysch formations, which are key to understanding the area's stratigraphy and tectonic evolution (Figure 4).



Figure 4. (**a**) Massive sandstones overlaying fine-grained mudstones. (**b**) Typical exposure of mud-dominated flysch facies.

Remote Sensing Data

Regarding remote sensing data, we utilized Landsat 8 Collection 2 Level 2 (LC08/C02/T1_L2) images from the Google Earth Engine (GEE) platform to analyze the area of interest (21.25°–21.5°E, 38.65°–38.95°N). The GEE is a powerful cloud-based platform that provides free access to a vast archive of multi-petabyte geospatial datasets, including Earth observation imagery, weather, climate data, and Digital Elevation Models spanning four decades [57]. The preprocessing included (a) the radiometric scaling process of the optical zones on the reflectance surface, (b) the process of selecting images with low cloud cover and specifically using the QA_PIXEL zone and (c) the creation of an annual average composite to represent surface conditions. Following the preprocessing phase, we produced a False Color Composite (FCC), which was created using bands 7, 5, and 4 (SWIR2, NIR, and Red) to highlight water bodies, vegetation, and geological units. Afterwards, processing techniques such as Principal Component Analysis (PCA) and Minimum Noise Fraction (MNF) transformations were applied, with the first three components of each (PCA1, PCA2, and PCA3 and MNF1, MNF2, and MNF3) being used to extract the most important spectral and noise-reduced features.

To ensure thorough analysis, the dataset was filtered by date (from 1 January 2021 to 31 December 2021) and location, followed by preprocessing steps to produce cloud-free composites. A total of 44 images were obtained. For each product, FCC, PCA, and MNF, the mean reflectance was computed across the visible, near-infrared, and shortwave infrared bands (B2–B7) over the course of the year. The preprocessing involved scaling reflectance data, masking clouds and shadows using the QA_PIXEL band, and clipping the dataset to match the specified area of interest.

Specifically, the Dissection Index (DI) is a geomorphological metric derived from a Digital Elevation Model (DEM) to quantify the degree of topographic dissection within a given area [58,59]. It reflects the intensity of terrain segmentation by analyzing the interplay of elevation changes and slope characteristics [60,61]. The DI is particularly useful for identifying areas of high geological and structural complexity, such as ridges, valleys, and escarpments, which are often indicative of underlying lithological and tectonic features. To extract the DI, we used the ALOS Phased Array type L-band Synthetic Aperture Radar

(PALSAR). PALSAR is an advanced interferometric radar (InSAR) system designed for high-resolution applications such as topography launched in 2006 by JAXA and JAROS [62]. Operating in ScanSAR mode, PALSAR captures images 250–350 km wide—three to five times broader than conventional SAR images—while maintaining a fine spatial resolution of 12.5 m and 16-bit quantization. Its coverage spans 60°N to 59°S, with associated DEMs released between 2014 and 2015 [63].

False Color Composites (FCCs) serve as an essential preliminary processing technique to visualize the general features of an area [27]. In this study, FCCs were employed to distinguish lithological units, including Holocene geological units, mud-dominated flysch, sand-dominated flysch, and Cretaceous limestones, as delineated by the geological map. Landsat bands were utilized effectively, with Band 7 (SWIR2), known as the geology band, for mineral and lithological detection, Band 5 (NIR) for soil and rock discrimination, and Band 4 (Red) for distinguishing vegetation from exposed rock or soil [64,65].

Principal Component Analysis (PCA) is a multivariate statistical technique used for dimensionality reduction and spectral enhancement in remote sensing applications [66,67]. Performing this process allows for the extraction of cartographic products that emphasize geological features by reducing data redundancy and suppressing radiation effects in Multispectral Instrumentation (MSI) bands [68]. The basic process of PCA is to transform correlated spectral bands into linearly uncorrelated principal components (PCs) by computing covariance and correlation matrices, defining new orthogonal axes that capture the variation within the dataset [69].

Minimum noise fraction (MNF) analysis is one of the most widely used techniques for satellite image denoising [70]. The MNF technique is particularly valuable for geological applications, since it is possible to extract informative data while separating noise, thus improving the quality of the dataset. The MNFA process involves two sequential principal component transformations [70,71]: noise whitening, the initial step, which uses the noise covariance matrix to decorrelate and rescale the noise in the dataset, effectively separating the noise from the important spectral information, and principal component transformation. The latter process involves a PCA transformation of the noise-whitened data, organizing the information into components ranked by their eigenvalues. The bands with the highest eigenvalues are retained for further processing, as they contain the most significant variance in the dataset, avoiding redundancy.

2.2.2. Training and Validation Database

The study area was divided into two distinct regions, a and b (Figure 5), to evaluate the performance of the different models under different conditions mainly in terms of the presence of different geological formations. This procedure ensures that the predictive models were trained on known lithologies and evaluated in areas that were completely excluded from the training process. In more detail, the first region, region a, is covered by water bodies, Holocene geological units that, according to the geological map, are characterized as landslides, mud-dominated flysch, sand-dominated flysch, and Cretaceous limestones, while the second region, region b, is covered with mud-dominated flysch and sand-dominated flysch.

Regarding the subsequent learning process, the research area was divided into 128 × 128-pixel patches with a step size of 64 pixels, ensuring overlap to capture outliers and reduce the effect thresholds during model training. The input data, as mentioned, consisted of a 10-band data stack, including DEM, FCC, MNF, and PCA, providing multispectral and morphology information for the lithological classification process. The corresponding labels were derived from the geological map, which was verified in areas by field surveys. In region a, the dominant formation is sand-dominated flysch, covering

37% of the area, followed by mud-dominated flysch at 34% and water bodies at 26%. The Cretaceous limestone and landslides each contribute minimally, accounting for just 2% each. In region b, the lithology is simpler, with mud-dominated flysch dominating 74% of the area, while sand-dominated flysch covers the remaining 26%.

In order to address potential problems raised by the presence of unbalanced training datasets, the models were optimized with focal loss. For each training region, 80% of the produced patches were randomly selected for the training dataset, while the remaining 20% were used for testing. To enhance the diversity and robustness of the training samples, data augmentation techniques were applied, including 90°, 180°, and 270° rotations [72]. This augmentation process effectively increased the size and variability of the training dataset, allowing the model to better generalize different lithological patterns and spatial orientations. Concerning the possibility of lithological classes to be distinguished by remote sensing data, water bodies may be identified by low reflectance in visible/near-infrared bands and flat DEM indices [73], whereas landslide bodies may be identified by their irregular slope and roughness patterns with unique spectral signatures in FCC and PCA composites. Cretaceous limestones may be clearly identified by its distinctive spectral absorption features in shortwave infrared bands, whereas mud-dominated flysch formations typically exhibit lower reflectance in visible and shortwave infrared (SWIR) bands due to their clay-rich composition and higher moisture retention, and sand-dominated flysch formations show higher reflectance in visible and SWIR bands, attributed to their quartz-rich content [74].

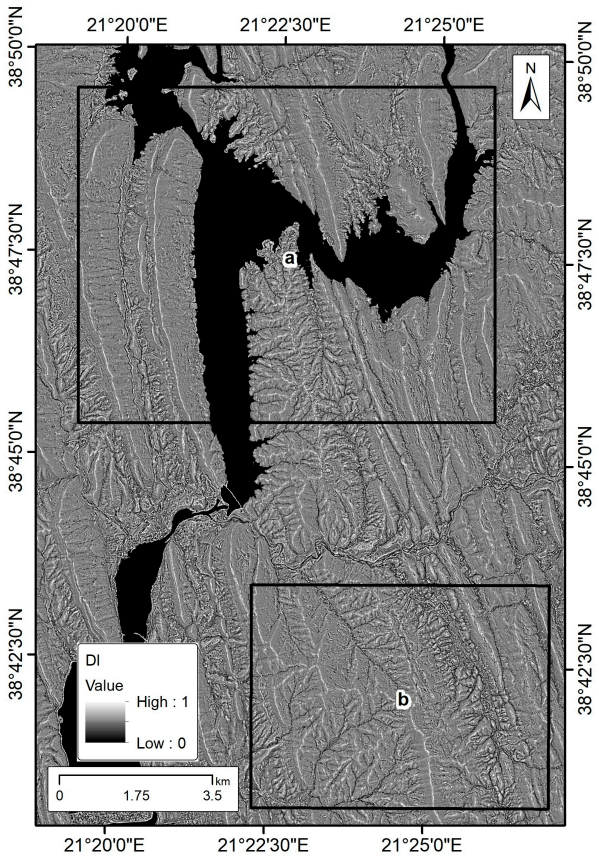


Figure 5. *Cont.*

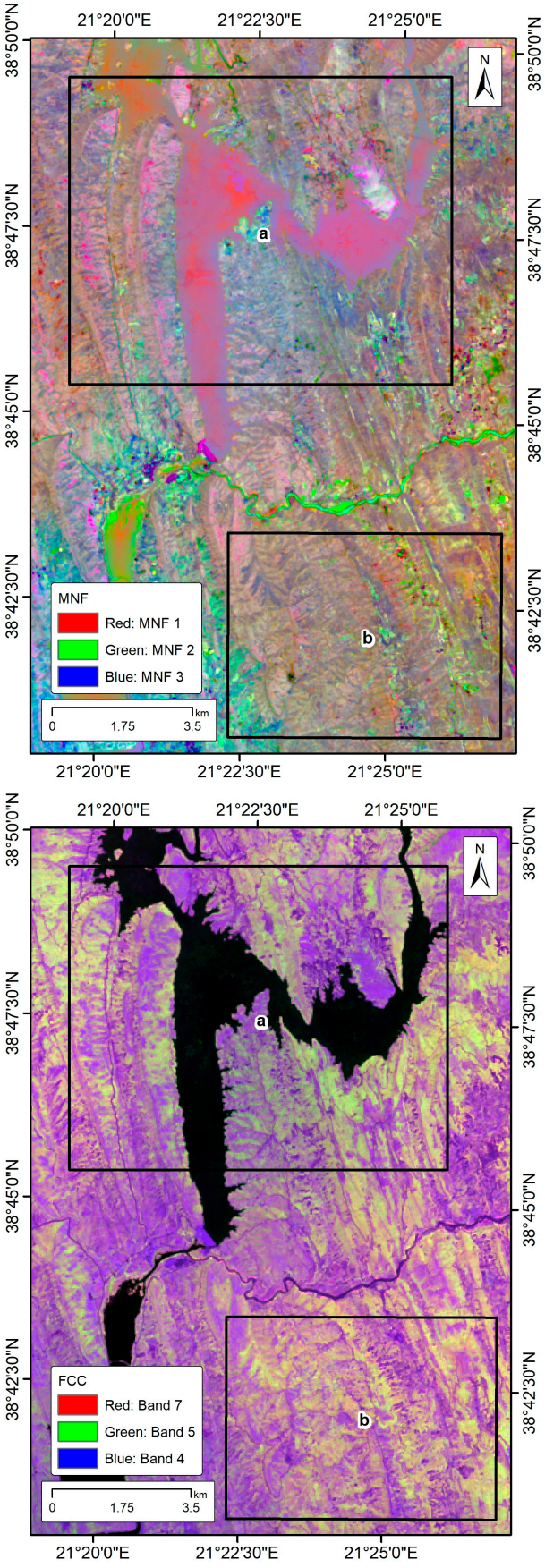


Figure 5. *Cont*.

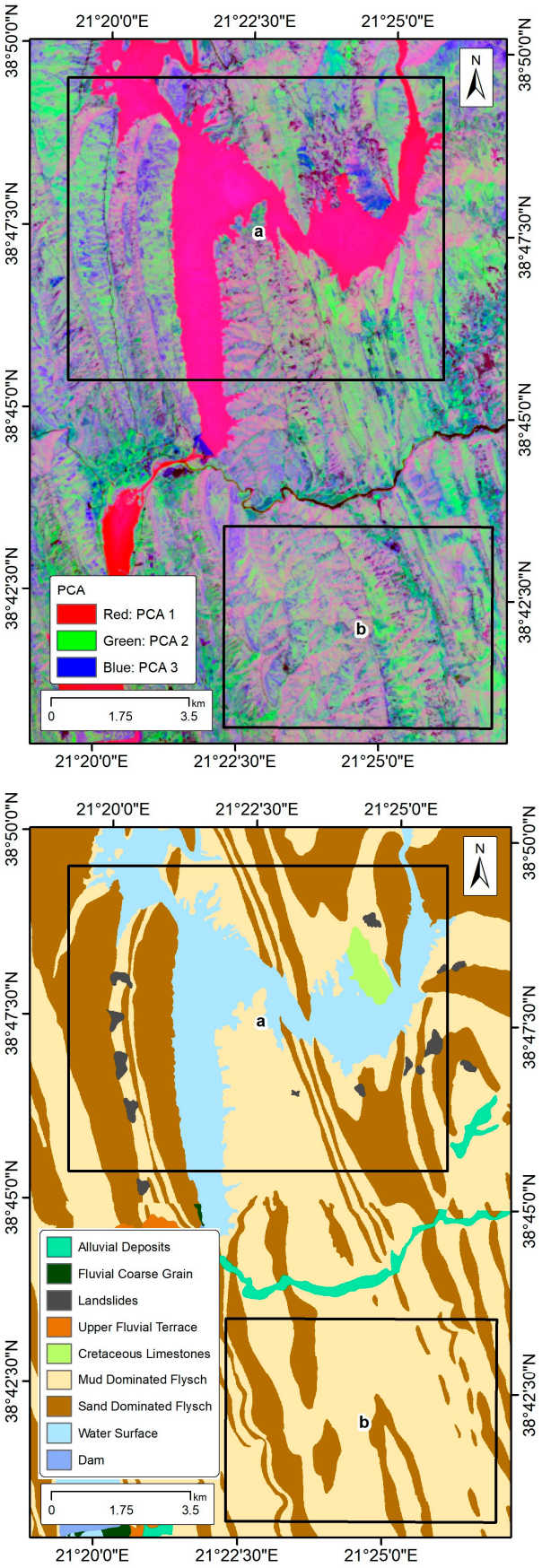


Figure 5. Regions a and b overlaid on the Dissection Index map, False Color Composite (FCC), Principal Component Analysis (PCA), Minimum Noise Fraction (MNF), and the ground truth geological map, illustrating the specific areas used for model development and performance evaluation.

2.2.3. Implementation of U-Net Models

The U-Net concept, proposed by Ronneberger et al. [21], represents an evolved Fully Convolutional Network model characterized by its symmetrical U-shaped architecture, which includes distinct contracting and expanding paths. The contracting path is designed to capture contextual information, while the expanding path focuses on the precise localization of segmented objects. U-Net effectively integrates low-level features containing spatial information from the contracting path with high-level semantic features from the expanding path, enhancing the segmentation accuracy [23]. Successive convolutional layers are trained to refine outputs and improve reliability based on this integrated information. Leveraging semantic segmentation techniques, U-Net models efficiently learn spatial relationships between land cover classes [25], enabling the superior classification of objects across entire images, particularly when labeled data are limited. Furthermore, when discontinuities arise in predictions due to noise in the labeled data, these models inherently perform a regularization process that acts as a post-processing smoothing step [26]. This combination of contextual and spatial understanding makes U-Net a robust choice for semantic segmentation tasks. The U-shaped architecture has gained significant attention for its application in object detection, particularly using remote sensing data [75]. In our study, we utilized advanced variants of the U-Net architecture, including Dense U-Net, Residual U-Net, and Attention U-Net, to further enhance the segmentation accuracy and performance.

Dense U-Net

Dense U-Net combines the strengths of U-Net's encoder–decoder architecture and DenseNet's dense connectivity to create an efficient, end-to-end semantic segmentation network [76]. The U-shaped structure of Dense U-Net ensures multi-scale feature extraction and progressive upsampling, while the dense connections reuse features across layers, enhancing gradient flow and reducing redundancy. Each layer in the dense blocks is directly connected to all preceding layers, allowing effective information propagation and improved feature reuse [77]. This design enables precise detail restoration, making Dense U-Net particularly suitable for tasks requiring high-resolution segmentation, such as medical imaging, geospatial analysis, and object segmentation in complex environments.

Residual U-Net

U-Net-ResNet combines the U-Net architecture with a ResNet (Residual Network) backbone, enhancing its feature extraction capability through residual learning. The ResNet backbone allows the model to learn deeper and more complex features by mitigating issues like vanishing gradients [78]. This hybrid model is particularly effective for challenging geological mapping tasks, where subtle spectral and spatial variations require robust feature extraction. U-Net-ResNet is well suited for segmenting highly detailed geological formations, providing improved accuracy and generalization compared to standard U-Net [79].

In our case, the modified U-Net includes four encoder blocks for downsampling, a bottleneck layer, and four decoder blocks for upsampling, with skip connections preserving spatial details. The architecture is trained using focal loss, which focuses on challenging examples to address class imbalance, and optimized with the Adam optimizer, while the training process monitors accuracy and validation loss across 100 epochs.

Attention U-Net

Attention U-Net is an enhanced variant of the U-Net architecture designed to focus on the most relevant regions of an input image while performing segmentation tasks. This

model incorporates attention mechanisms into the traditional U-Net framework, allowing the network to selectively emphasize important features while suppressing irrelevant ones [80]. These attention gates (AGs) are integrated into the skip connections between the contracting and expanding paths, dynamically filtering the features being transferred to the decoder. By doing so, the model improves the precision of segmentation by concentrating on salient regions that are critical for the task at hand.

This enhancement is particularly advantageous when working with complex or noisy datasets, as the attention mechanism reduces the influence of background noise and irrelevant details. In addition, Attention U-Net retains the core strengths of the original U-Net architecture, such as its encoder–decoder structure and symmetric design, while delivering improved performance in terms of accuracy and feature localization. Its ability to highlight relevant spatial and semantic features makes it especially effective in applications like medical image analysis, where precise segmentation is crucial.

2.2.4. Validation and Final Mapping

To evaluate the performance of U-Net-based models, accuracy (Acc), precision (Pre), recall, F1-score, and intersection over union (IoU) were applied [81]. Regarding the metric accuracy, it measures the percentage of correctly segmented pixels, while precision evaluates the proportion of correctly identified pixels compared to the total pixels classified by the model. The recall index quantifies the ability of the examined model to detect all relevant pixels in the ground truth. The F1-score is an index that balances precision and recall, emphasizing accuracy in marginal regions [82]. Finally, the IoU index, or Jaccard similarity index, is considered the most critical metric for segmentation, assessing the overlap between model predictions and ground truth, providing a direct measure of the model's accuracy in terms of spatial alignment [83,84].

3. Results

For the first region (Figure 6), each model performed sufficiently well (Table 1). In particular, the Attention U-Net model achieved an overall accuracy of 0.9595, followed by the Residual U-Net model, which achieved 0.9247, and the Dense U-Net, which achieved 0.8993. Similarly, regarding the IoU metric, Attention U-Net, with a value of 0.9320, outperformed the Dense U-Net (0.8517) and Residual U-Net model (0.7459).

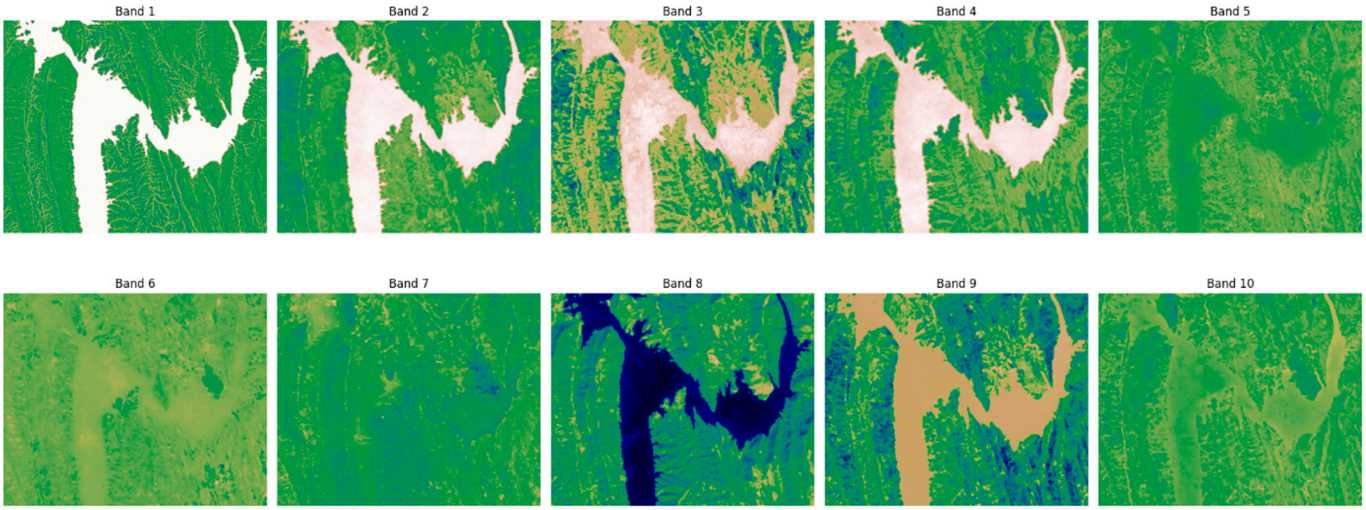


Figure 6. Visualization of region a using 10 spectral bands, incorporating the Dissection Index map, False Color Composite (FCC), Principal Component Analysis (PCA), and Minimum Noise Fraction (MNF) transformations.

Table 1. Statistical metrics of accuracy and IoU for the testing database—region a.

Models	Overall Accuracy %	Overall IoU %
Dense U-Net	0.8993	0.7459
Residual U-Net	0.9247	0.8517
Attention U-Net	0.9597	0.9320

Concerning the performance of the models in respect to the different units that cover the first region, all the models have a high accuracy value for water body classification, with Attention U-Net achieving near-perfect results (F1-score: 0.9851). Residual U-Net followed with a slightly lower performance (F1-score: 0.9645) (Table 2). The Dense U-Net model achieved its highest F1-score in this category, almost as well as the other models in this category (F1-score: 0.9581). Such a performance could be explained by the fact that, in general, water bodies typically exhibit distinct and easily separable features due to their uniform spectral and spatial characteristics, such as consistent reflectance values and a lack of texture compared to other geological formations.

Table 2. Statistical metrics of accuracy and mIoU for the testing database—region a.

Models	Landslide Body	Cretaceous Limestone	Mud-Dominated Flysch	Sand-Dominated Flysch	Water Body
Dense U-Net	Precision: 0.7282 Recall: 0.3765 F1-score: 0.4964	Precision: 0.9717 Recall: 0.8871 F1-score: 0.9274	Precision: 0.9043 Recall: 0.8384 F1-score: 0.8701	Precision: 0.8737 Recall: 0.9628 F1-score: 0.9161	Precision: 0.9589 Recall: 0.9573 F1-score: 0.9581
Residual U-Net	Precision: 0.8511 Recall: 0.8607 F1-score: 0.8559	Precision: 0.9610 Recall: 0.9345 F1-score: 0.9476	Precision: 0.9298 Recall: 0.8610 F1-score: 0.8941	Precision: 0.9072 Recall: 0.9553 F1-score: 0.9307	Precision: 0.9547 Recall: 0.9744 F1-score: 0.9645
Attention U-Net	Precision: 0.9979 Recall: 0.9365 F1-score: 0.9662	Precision: 0.9741 Recall: 0.9963 F1-score: 0.9851	Precision: 0.9784 Recall: 0.8918 F1-score: 0.9331	Precision: 0.9208 Recall: 0.9870 F1-score: 0.9528	Precision: 0.9798 Recall: 0.9904 F1-score: 0.9851

Sand-dominated and mud-dominated flysch formations are considered as a more challenging classification task compared to water bodies, since they have similar spectral and textural characteristics. Despite these complexities, the models demonstrate varying levels of performance, with the Attention U-Net and Residual U-Net showing superior F1-scores compared to those of the Dense U-Net.

Cretaceous limestone, despite its relatively smaller surface coverage compared to the sand- and mud-dominated flysch formations, achieves high classification accuracy across all models. This can be attributed to its distinct spectral and textural properties, which allow for easier differentiation from other geological units. The Attention U-Net demonstrates exceptional performance, achieving the highest F1-score (0.9851) by effectively leveraging attention mechanisms to focus on the subtle but critical features of this unit. The Residual U-Net also performs well, with an F1-score of 0.9476, utilizing its residual connections to enhance the representation of these distinct features. The Dense U-Net, while slightly less effective (F1-score: 0.9274), still achieves commendable results due to the relatively clear boundaries and unique spectral signature of Cretaceous limestone.

The landslide body unit, characterized by very small surface coverage, presents a significant challenge for classification due to its limited spatial extent and potential spectral overlap with surrounding formations. Among the models, the Attention U-Net achieves an outstanding performance, with a near-perfect precision (0.9979) and the highest F1-score (0.9662). Its attention mechanisms allow it to focus on critical, localized features, effectively handling the small and scattered nature of the landslide body.

The training and validation accuracy and loss curves for the three models, as presented in Figures 7 and 8, reveal distinct learning behaviors and convergence characteristics for region a. The Dense U-Net model demonstrates clear signs of overfitting, with a training accuracy exceeding 90% and training loss nearing zero, while the validation accuracy lags significantly and validation loss fails to plateau, reflecting poor generalization to unseen data. The Residual U-Net model improves generalization, with a smaller gap between training and validation accuracies, which stabilize around 95% and slightly lower, respectively, supported by consistent loss curve declines that highlight effective learning. The Attention U-Net model achieves the best performance, with the training accuracy nearing 99% and validation accuracy stabilizing around 96–97%, accompanied by minimal divergence between training and validation losses, indicating excellent generalization and robust learning dynamics.

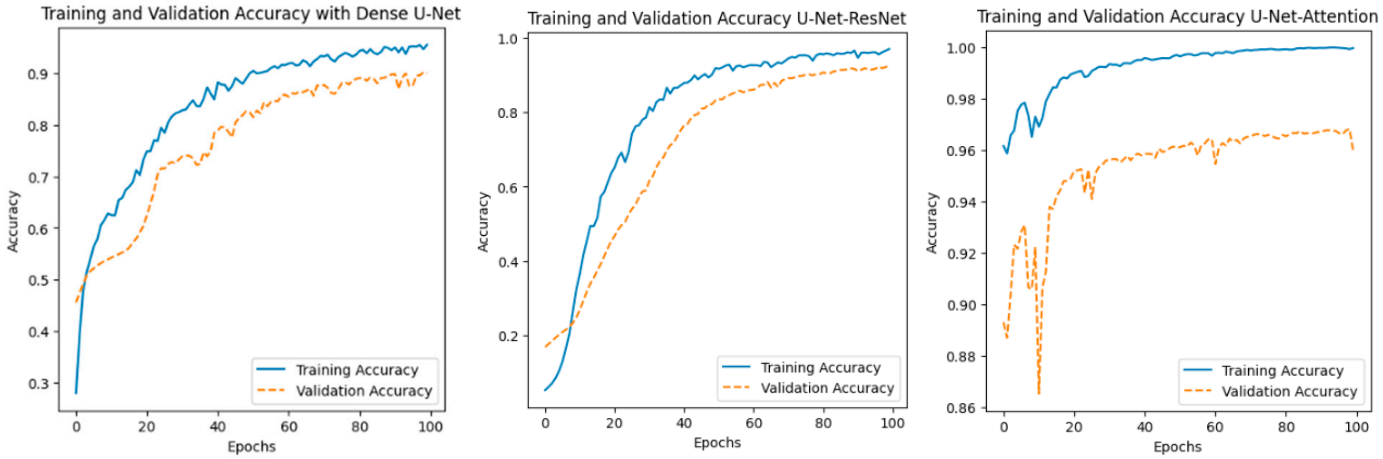


Figure 7. Training and validation accuracy curves for the three models concerning region a.

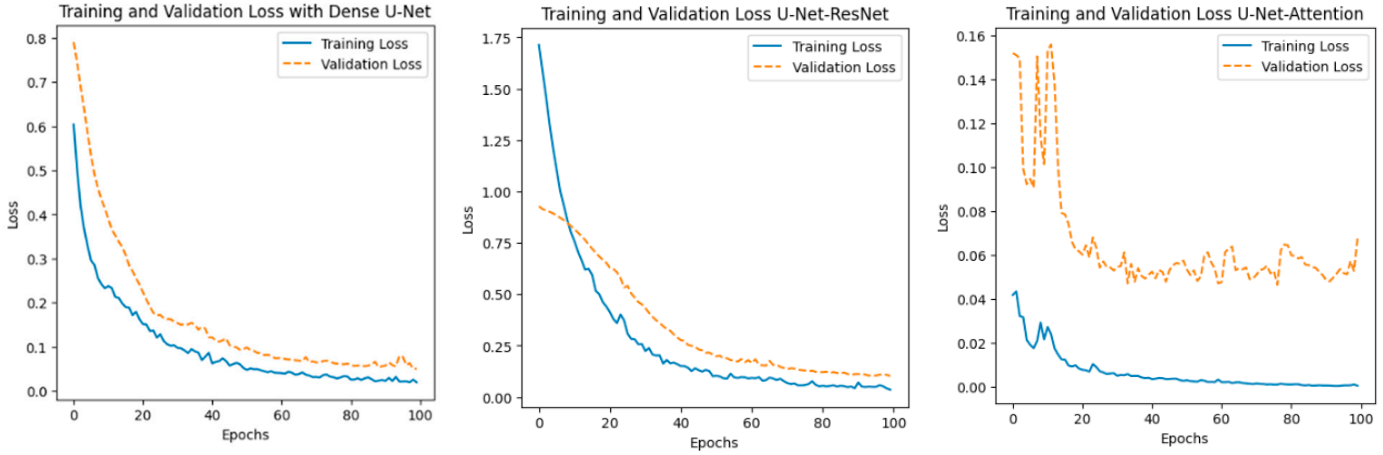


Figure 8. Training and validation loss curves for the three models concerning region a.

Figure 9 illustrates the overall prediction map in region a based on the three models. Compared to the ground truth geological map, the Attention U-Net model produced the smoothest outcome. In more detail, Dense U-Net struggles with fine-grained details near boundaries, often blending or misclassifying transitions between classes such as water bodies and flysch formations, indicating limitations in capturing contextual features. ResNet U-Net improves edge predictions with smoother transitions and fewer misclassifications, leveraging residual connections to retain spatial information. Attention U-Net consistently outperforms the others, providing sharp, well-defined boundaries and minimal misclassifications, demonstrating its ability to focus on critical features in complex regions.

Overall, while the Dense U-Net and ResNet U-Net perform adequately in homogenous regions, their accuracy diminishes near boundaries, whereas the Attention U-Net excels in both edge-sensitive areas and overall alignment with the ground truth lithology map, underscoring the value of attention mechanisms for boundary-focused tasks.

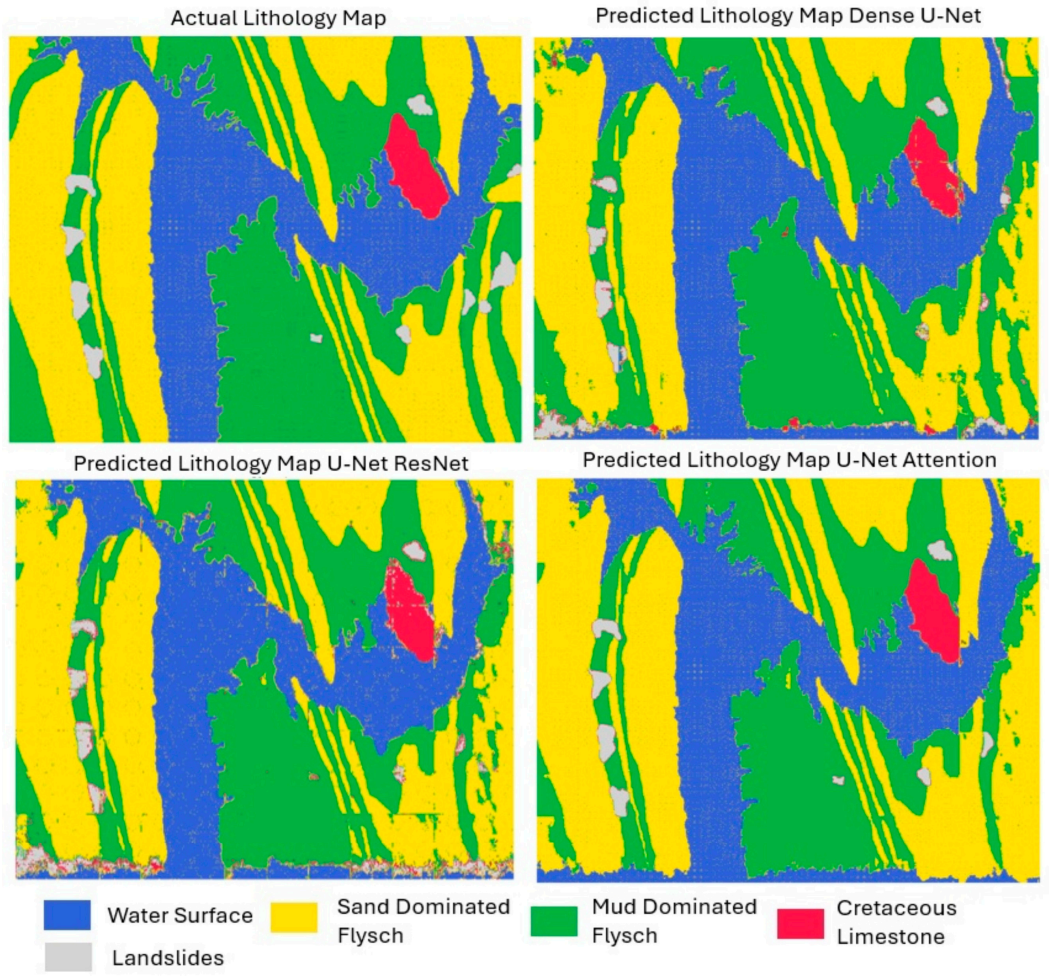


Figure 9. Ground truth lithology with the predicted lithology for region a, as determined by the three models.

The second region, region b, consists of only two lithological formations, the mud-dominated flysch and the sand-dominated flysch (Figure 10).

The performance comparisons among three U-Net model variants—Dense U-Net, Residual U-Net, and Attention U-Net—reveal distinct trends in the segmentation accuracy and IoU for region b (Table 3). Attention U-Net consistently leads the group, achieving an impressive overall accuracy of 98.77% and an IoU of 93.20%, underscoring its superior segmentation capabilities. Residual U-Net follows with a strong accuracy of 96.83% and an IoU of 90.66%, reflecting a reliable performance but slightly trailing the leader. Dense U-Net, while competent, ranks third with an accuracy of 94.76% and an IoU of 87.29%, indicating room for improvement.

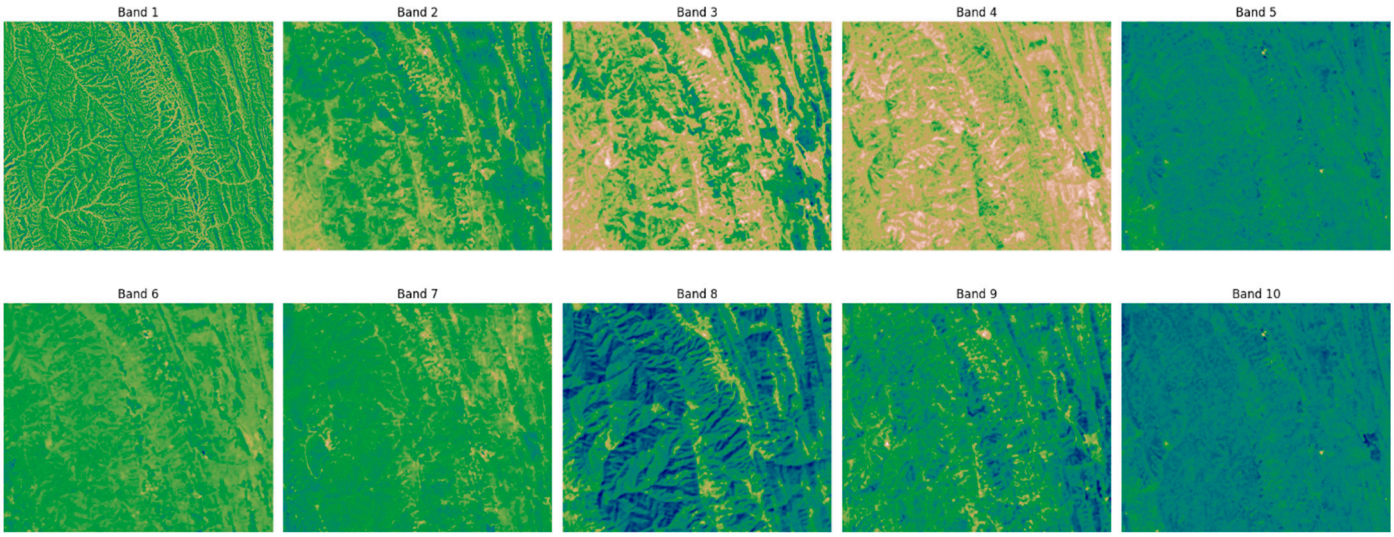


Figure 10. Visualization of region b using 10 spectral bands, incorporating the Dissection Index map, False Color Composite (FCC), Principal Component Analysis (PCA), and Minimum Noise Fraction (MNF) transformations.

Table 3. Statistical metrics of accuracy and IoU for the testing database—region b.

Models	Overall Accuracy %	Overall IoU %
Dense U-Net	0.9476	0.8729
Residual U-Net	0.9683	0.9066
Attention U-Net	0.9877	0.9320

For specific classes, Attention U-Net continues to excel, delivering outstanding F1-scores of 0.9921 for mud-dominated flysch and 0.9719 for sand-dominated flysch, demonstrating an excellent balance between precision and recall (Table 4). Residual U-Net also performs well, achieving F1-scores of 0.9783 and 0.9223 for the same classes, though its precision for sand-dominated flysch is slightly lower. Dense U-Net exhibits a noticeable decline in performance for sand-dominated flysch, where its F1-score drops to 0.8908.

Table 4. Statistical metrics of accuracy and mIoU for the testing database—region b.

Models	Mud-Dominated Flysch	Sand-Dominated Flysch
Dense U-Net	Precision: 0.9582 Recall: 0.9834 F1-score: 0.9706	Precision: 0.9359 Recall: 0.8489 F1-score: 0.8908
Residual U-Net	Precision: 0.9732 Recall: 0.9835 F1-score: 0.9783	Precision: 0.9401 Recall: 0.9051 F1-score: 0.9223
Attention U-Net	Precision: 0.9876 Recall: 0.9967 F1-score: 0.9921	Precision: 0.9882 Recall: 0.9561 F1-score: 0.9719

In region B, which involves the simpler classification of two lithological units (mud-dominated flysch and sand-dominated flysch), all models exhibit improved generalization compared to region A, as reflected in their training and validation accuracy and loss curves (Figure 11). Dense U-Net achieves a training accuracy above 90%, with the validation accuracy closely following, though a slight gap remains, indicating minor overfitting. Its training loss decreases smoothly but stabilizes slightly below the validation loss, reflecting constrained generalization. The Residual U-Net model demonstrates a stronger performance, with a training accuracy surpassing 95% and validation accuracy closely mirroring

it, while its loss curves align well, highlighting effective learning dynamics and improved generalization due to residual connections (Figure 12). Attention U-Net outperforms both, with a training accuracy near 99% and validation accuracy stabilizing at 98%, accompanied by minimal gaps between the training and validation losses, showcasing exceptional generalization and negligible overfitting. Overall, the simpler task in region B allows all the models to perform better, but Attention U-Net consistently leads with the highest accuracy, lowest loss, and the most robust generalization. Residual U-Net follows as a strong contender, while Dense U-Net, though improved, still exhibits slight limitations in generalization.

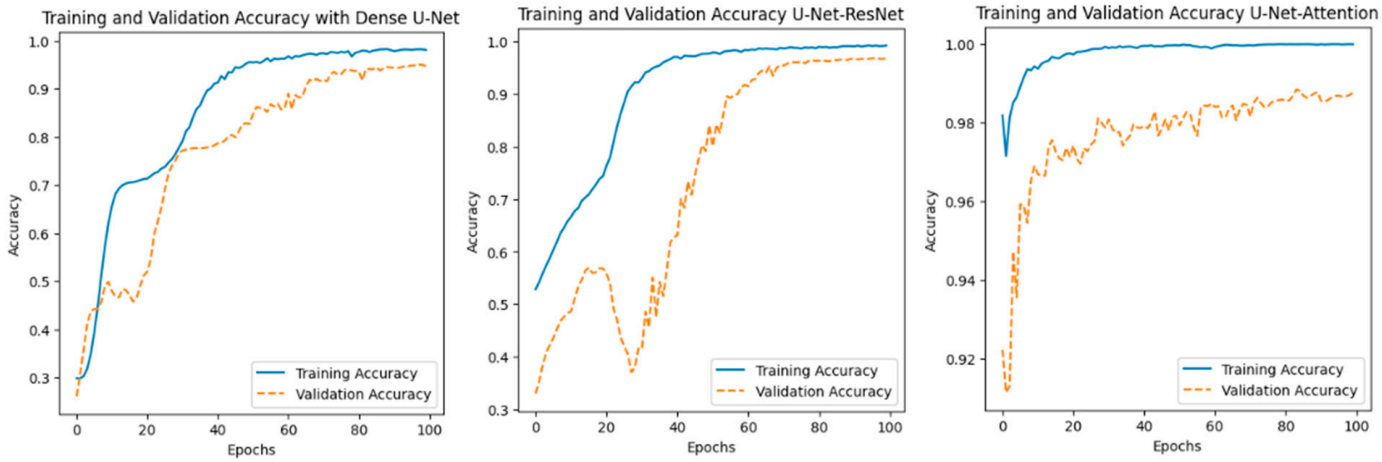


Figure 11. Training and validation accuracy curves for the three models concerning region b.

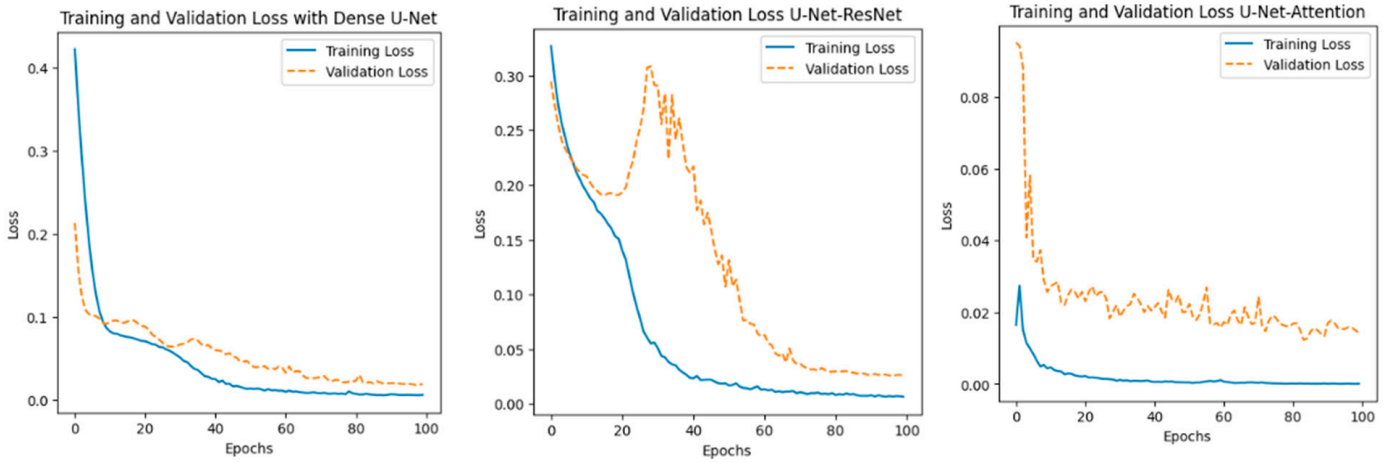


Figure 12. Training and validation loss curves for the three models concerning region b.

Concerning the predicted lithological map and in the case of region b, the Dense U-Net model produces predictions that resemble the ground truth; however, similarly to the outcome of region a, it struggles with edge refinement, showing, in some cases, blending and misclassifications at transitions between the mud-dominated flysch and sand-dominated flysch formations, likely due to its limited capacity for detailed spatial information retention (Figure 13). The Residual U-Net model improves edge definition, with more distinct boundaries and better alignment with the ground truth, benefiting from residual connections that preserve spatial features across layers, though minor inaccuracies persist. The Attention U-Net model achieves again the best performance, delivering sharp and precise boundaries with smooth transitions, thanks to its attention mechanisms that focus effectively on critical features, especially near edges.

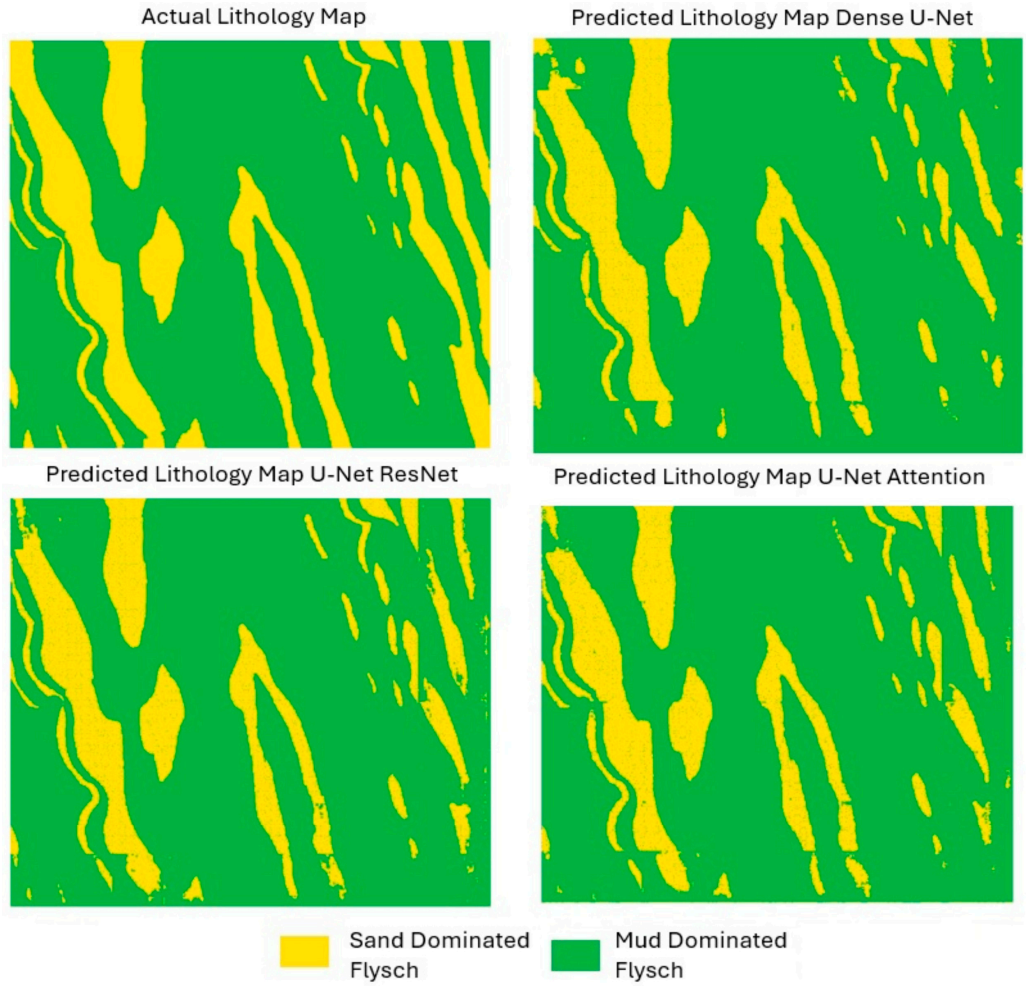


Figure 13. Ground truth lithology with the predicted lithology for region b, as determined by the three models.

4. Discussion

In the initial phases of geological interpretation using remote sensing images, visual interpretation was the primary method employed, which, however, relied heavily on the expertise and field experience of professional geologists, making it inherently subjective and limiting its effectiveness for large-scale lithological mapping [85]. In recent years, widely utilized datasets for remote sensing lithology identification and integrating data from multiple sources have provided valuable information, which have significantly enhanced the accuracy and efficiency of lithological mapping [86]. Similarly, Blaschke et al. [87] highlights that the integration of texture features in remote sensing applications has significantly improved the classification results, with this improvement mainly due to the use of object-based segmentation techniques that incorporate both spatial and spectral information, rather than relying solely on pixel-based analysis. This is also agreed on by Pandey et al. [88], who, in turn, point out that this approach leads to more efficient classifications. Furthermore, advances in computing power in recent years, as discussed by Ma et al. [89], have allowed CNNs to achieve a higher classification accuracy compared to traditional methods such as support vector machines (SVMs) and random forests (RFs). This is emphasized in further research by Ma et al. [90], highlighting the superiority of CNNs in handling complex remote sensing data for classification tasks. The combination of advanced neural network architectures as well as increased computational capabilities has significantly pushed the boundaries of accuracy and efficiency in remote sensing classifications [91].

The results of our developed methodology demonstrate the possibility of co-evaluating spectral, topographic, and computational methodologies for the discrimination of lithological phases of flysch formations with particularly high accuracy. In particular, the co-evaluation of CRC, PCA, and MNF provided distinct and complementary spectral information, mainly highlighting the subtle differences in the mineralogical composition and lithological boundaries. In addition, the DI was used as an index with additional topographic information, especially in areas where the lithology is closely related to geomorphic patterns, as is the case in our region. The above constituted input data, which were considered decisive due to their ability to represent spectral and spatial features, enriching the training datasets for the deep learning models.

Comparing both regions, Attention U-Net emerges as the most robust model, excelling in both complex and simpler tasks. Residual U-Net consistently ranks second, offering a dependable performance across varying complexities. Dense U-Net, while effective in less challenging scenarios, struggles with highly complex classes, particularly in region a. A broader trend highlights the inverse relationship between the model performance and class complexity. In region a, the greater diversity and spectral overlap among classes—such as the mud-dominated and sand-dominated flysch—and the limited spatial extent of certain units, like landslide bodies, pose significant challenges. As a result, all models show lower accuracy, IoU, and F1-scores compared to those of region b. Attention U-Net's ability to focus on critical features through its attention mechanisms gives it a clear advantage in handling these challenges. In contrast, the simpler classification task in region b allows all models to perform better, with the accuracy and IoU improving across the board. This underscores that models with simpler architectures, like Dense U-Net, can achieve solid results when the classification complexity is lower. However, the Attention U-Net model remains the top performer across both regions, demonstrating superior adaptability and resilience to varying levels of complexity.

The performance of segmentation models, such as the CNN U-Net-based model, can vary significantly depending on the complexity of the classification task [92]; in our case, this was true for the lithological classification task, particularly when comparing areas with only two lithologies to those with five geological formations. In regions with only two lithologies, the classification task is relatively simple, as the model needs to differentiate between just two classes. This simplicity often results in high accuracy and reduced class confusion, allowing even simpler architectures like U-Net or 2D-CNN to perform well. The reduced class complexity also minimizes the risk of overfitting and improves generalization. However, when dealing with five geological formations, the task becomes much more complex due to increased spectral similarity and overlapping spatial features between classes, such as sand-dominated and mud-dominated flysch. This scenario demands more advanced feature extraction capabilities to accurately distinguish between classes. While simpler models may suffice for binary classification tasks, multi-class scenarios with diverse lithologies highlight the advantages of Attention or Residual U-Net models in handling class imbalance, subtle spectral differences, and preserving spatial details. This comparison underscores the importance of aligning model selection with task complexity to achieve optimal performance in lithological mapping.

In more detail, the Dense U-Net model captures the broad structures of the lithological units, but struggles with smaller or less distinct features, such as areas that geological maps have identified as landslides, which appear fragmented or inaccurate due to its limitations in emphasizing fine details and separating overlapping features. In contrast, Residual U-Net, with its residual connections, demonstrates improved delineation and consistent pattern prediction, particularly for transitions between geological units and landslide bodies, reflecting its ability to extract deeper features. Finally, the Attention

U-Net outperforms the other models by incorporating attention gates, allowing it to focus on critical features. This results in the most accurate segmentation, effectively handling small or demanding units such as landslide bodies and excelling in capturing complex geological boundaries and spatial details.

Despite the high performance achieved during the application of the modified U-Net-based models, its implementation presents some limitations. The main limitation is the potential geological complexity that an area of interest may present, as, in our case, the analysis focused on an area characterized by relatively stable geological characteristics. The increase in the number of distinct geological formations may affect the accuracy and reliability of the model. In addition, the quality of the ground truth data and the availability of representative samples are critical factors affecting the accuracy of the model and inconsistencies or gaps in these data sources could lead to a reduced predictive performance. Another point that should be mentioned is that the U-Net architecture and its variants show strong capabilities for pixel-level segmentation; however, the complexity of the geological distribution may require further improvement in feature extraction and representation to fully capture complex geological patterns. As mentioned by Clark et al. [23], the effectiveness of a U-Net model in Earth observation tasks depends on the careful balance and selection of these architectural and algorithmic elements, which require thorough experimentation and validation. In this case, it is important to consistently perform thorough data preprocessing, adopt more efficient feature engineering techniques, and carry out precise model tuning to ensure the accurate mapping of geological formations.

Regarding the possible future studies that could be implemented to address the limitations to some extent, they should prioritize expanding the dataset to include a wider range of geological formations. In this direction, the use of adaptive learning and transfer learning techniques could allow models to better generalize to areas with different geological characteristics, especially those with limited data [81]. In addition, the application of optimization strategies such as regularization, dropout, and batch normalization can help improve performance and avoid overfitting, especially when working with smaller datasets. Another promising direction for future research is the incorporation of time series analysis or geo-spatiotemporal modeling as input data to exploit dynamic geological changes, such as erosion, tectonic displacements, and sediment deposition. These processes vary in dynamics and intensity depending on the host geological formation on which they occur.

5. Conclusions

This present study demonstrates the effectiveness of integrating remote sensing techniques with U-Net-based deep learning models for lithology mapping in complex terrains. Using Landsat 8 imagery, ALOS PALSAR data, and derived products such as FCC, PCA, MNF transformations, and the Dissection Index, as a morphological index, the methodology provided reliable inputs for accurate lithological classification. Validation metrics, including accuracy, precision, recall, F1-score, and IoU, enabled a detailed evaluation of three U-Net variants: Dense U-Net, Residual U-Net, and Attention U-Net. The findings highlight Attention U-Net as the most effective model, consistently outperforming the others in both complex and simpler lithological settings. It achieved the highest accuracy, IoU, and F1-scores, particularly excelling in edge-sensitive tasks and challenging formations such as mud-dominated and sand-dominated flysch, as well as landslide bodies. Its attention mechanisms facilitated precise feature extraction and boundary refinement, demonstrating superior robustness in handling diverse spectral and spatial complexities. Residual U-Net ranked second, with enhanced generalization and better edge refinement compared to Dense U-Net, owing to its residual connections that preserved critical spatial information.

Dense U-Net, though capable, struggled with fine-grained details and boundary transitions, making it less effective for complex classification tasks. This study also underscores the relationship between task complexity and model performance. In region A, which involved five lithological units with overlapping spectral and textural features, the model accuracy was generally lower, and the advantages of advanced architectures like Attention U-Net were more pronounced. In contrast, region B, with only two lithological units, presented a simpler classification task, allowing all models to perform better, though Attention U-Net continued to deliver the most accurate and precise predictions. The results emphasize the importance of attention mechanisms for improved feature extraction and edge refinement, especially in diverse and challenging regions. This approach has significant potential to advance geological mapping, and future research could explore incorporating additional data sources and further optimizing deep learning models to address a wider range of geological settings.

Author Contributions: Conceptualization, P.T. and I.V.; methodology, P.T.; formal analysis, P.T. and I.V.; investigation, I.V. and I.Z.; data curation, P.T. and I.V.; writing—original draft preparation, P.T., I.V. and I.Z.; writing—review and editing, P.T., I.V. and I.Z. All authors have read and agreed to the published version of the manuscript.

Funding: This research received no external funding.

Data Availability Statement: The original contributions presented in this study are included in the article. Further inquiries can be directed to the corresponding author.

Conflicts of Interest: The authors declare no conflicts of interest.

References

1. Peyghambari, S.; Zhang, Y. Hyperspectral Remote Sensing in Lithological Mapping, Mineral Exploration, and Environmental Geology: An Updated Review. *J. Appl. Remote Sens.* **2021**, *15*, 031501. [CrossRef]
2. Mahmood, T.; Hasan, K.; Akhter, S. Lithologic Mapping of a Forested Montane Terrain from Landsat 5 TM Image. *Geocarto Int.* **2018**, *34*, 750–768. [CrossRef]
3. Pal, M.; Rasmussen, T.; Porwal, A. Optimized Lithological Mapping from Multispectral and Hyperspectral Remote Sensing Images Using Fused Multi-classifiers. *Remote Sens.* **2020**, *12*, 177. [CrossRef]
4. Bachri, I.; Hakdaoui, M.; Raji, M.; Teodoro, A.C.; Benbouziane, A. Machine Learning Algorithms for Automatic Lithological Mapping Using Remote Sensing Data: A Case Study from Souk Arbaa Sahel, Sidi Ifni Inlier, Western Anti-Atlas, Morocco. *ISPRS Int. J. Geo-Inf.* **2019**, *8*, 248. [CrossRef]
5. Pour, A.B.; Hashim, M.; Hong, J.K.; Park, Y. Lithological and alteration mineral mapping in poorly exposed lithologies using Landsat-8 and ASTER satellite data: North-eastern Graham Land, Antarctic Peninsula. *Ore Geol. Rev.* **2019**, *108*, 112–133. [CrossRef]
6. Dong, Y.; Yang, Z.; Liu, Q.; Zuo, R.; Wang, Z. Fusion of GaoFen-5 and Sentinel-2B Data for Lithological Mapping Using Vision Transformer Dynamic Graph Convolutional Network. *Int. J. Appl. Earth Obs. Geoinf.* **2024**, *129*, 103780. [CrossRef]
7. Othman, A.A.; Gloaguen, R. Integration of spectral, spatial and morphometric data into lithological mapping: A comparison of different Machine Learning Algorithms in the Kurdistan Region, NE Iraq. *J. Asian Earth Sci.* **2017**, *146*, 90–102. [CrossRef]
8. Cracknell, M.J.; Reading, A.M. Geological mapping using remote sensing data: A comparison of five machine learning algorithms, their response to variations in the spatial distribution of training data and the use of explicit spatial information. *Comput. Geosci.* **2014**, *63*, 22–33. [CrossRef]
9. Sahoo, S.; Jha, M.K. Pattern recognition in lithology classification: Modeling using neural networks, self-organizing maps and genetic algorithms. *Hydrogeol. J.* **2017**, *25*, 311–330. [CrossRef]
10. El-Omairi, M.A.; El Garouani, A. Advancements in Lithological Mapping Utilizing Machine Learning Algorithms and Remote Sensing Data. *Heliyon* **2023**, *9*, e20168. [CrossRef]
11. Manap, H.S.; San, B.T. Data Integration for Lithological Mapping Using Machine Learning Algorithms. *Earth Sci. Inform.* **2022**, *15*, 1841–1859. [CrossRef]
12. Muzirafuti, A. Remotely Sensed and Field Data for Geomorphological Analysis of Water Springs: A Case Study of Ain Maarrouf. *Geosciences* **2024**, *14*, 51. [CrossRef]

13. Appiah-Twum, M.; Xu, W.; Sunkari, E.D. Mapping Lithology with Hybrid Attention Mechanism–Long Short-Term Memory: A Hybrid Neural Network Approach Using Remote Sensing and Geophysical Data. *Remote Sens.* **2024**, *16*, 4613. [CrossRef]
14. Kattenborn, T.; Leitloff, J.; Schiefer, F.; Hinz, S. Review on Convolutional Neural Networks (CNN) in Vegetation Remote Sensing. *ISPRS J. Photogramm. Remote Sens.* **2021**, *173*, 24–49. [CrossRef]
15. Wang, Z.; Zuo, R.; Liu, H. Lithological Mapping Based on Fully Convolutional Network and Multi-Source Geological Data. *Remote Sens.* **2021**, *13*, 4860. [CrossRef]
16. Sarker, I.H. Deep Learning: A Comprehensive Overview on Techniques, Taxonomy, Applications and Research Directions. *SN Comput. Sci.* **2021**, *2*, 420. [CrossRef]
17. Deng, L.; Yu, D. Deep Learning: Methods and Applications. *Found. Trends Signal Process.* **2014**, *7*, 197–387. [CrossRef]
18. Fu, G.; Liu, C.; Zhou, R.; Sun, T.; Zhang, Q. Classification for high resolution remote sensing imagery using a fully convolutional network. *Remote Sens.* **2017**, *9*, 498. [CrossRef]
19. Carranza-García, M.; García-Gutiérrez, J.; Riquelme, J. A Framework for Evaluating Land Use and Land Cover Classification Using Convolutional Neural Networks. *Remote Sens.* **2019**, *11*, 274. [CrossRef]
20. Tsangaratos, P.; Ilia, I.; Chrysafi, A.-A.; Matiatos, I.; Chen, W.; Hong, H. Applying a 1D Convolutional Neural Network in Flood Susceptibility Assessments—The Case of the Island of Euboea, Greece. *Remote Sens.* **2023**, *15*, 3471. [CrossRef]
21. Ronneberger, O.; Fischer, P.; Brox, T. U-net: Convolutional networks for biomedical image segmentation. In Proceedings of the International Conference on Medical Image Computing and Computer-Assisted Intervention, Munich, Germany, 5–9 October 2015; pp. 234–241.
22. Liu, P.; Wei, Y.; Wang, Q.; Chen, Y.; Xie, J. Research on Post-Earthquake Landslide Extraction Algorithm Based on Improved U-Net Model. *Remote Sens.* **2020**, *12*, 894. [CrossRef]
23. Clark, A.; Phinn, S.; Scarth, P. Optimised U-Net for Land Use–Land Cover Classification Using Aerial Photography. *PFG J. Photogramm. Remote Sens. Geoinf. Sci.* **2023**, *91*, 125–147. [CrossRef]
24. Liu, L.; Song, Z.; Zhou, P.; He, X.; Zhao, L. AI-based rock strength assessment from tunnel face images using hybrid neural networks. *Sci. Rep.* **2024**, *14*, 17512. [CrossRef] [PubMed]
25. Polat, A.; Keskin, İ.; Polat, Ö. Automatic Detection and Mapping of Dolines Using U-Net Model from Orthophoto Images. *ISPRS Int. J. Geo-Inf.* **2023**, *12*, 456. [CrossRef]
26. Chen, W.; Li, X.; Qin, X.; Wang, L. Geological Lithology Semantic Segmentation Based on Deep Learning Method. In *Remote Sensing Intelligent Interpretation for Geology*; Springer: Singapore, 2024. [CrossRef]
27. Ghoneim, S.M.; Hamimi, Z.; Abdelrahman, K.; Khalifa, M.A.; Shabban, M.; Abdelmaksoud, A.S. Machine learning and remote sensing-based lithological mapping of the Duwi Shear-Belt area, Central Eastern Desert, Egypt. *Sci. Rep.* **2024**, *14*, 17010. [CrossRef] [PubMed]
28. Le, Y.; Porwal, A.; Holden, E.-J.; Dentith, M.C. Towards Automatic Lithological Classification from Remote Sensing Data Using Support Vector Machines. *Comput. Geosci.* **2012**, *45*, 229–239. [CrossRef]
29. Vakalas, I.; Tripsanas, E.; Tzimeas, C.; Konstantopoulos, P. Sedimentary Characteristics and Basin Evolution of a Compartmentalized Foreland Basin—Internal Ionian Zone, Western Greece. *Energies* **2024**, *17*, 315. [CrossRef]
30. Underhill, J.R. Neogene and Quaternary Tectonics and Sedimentation in Western Greece. Ph.D. Thesis, University of Wales, Cardiff, UK, 1985.
31. Aubouin, J. Contribution à l'Étude Géologique de la Grèce Septentrionale: Le Confins de l'Épire et de la Thessalie. *Ann. Géologiques Pays Helléniques* **1959**, *10*, 525.
32. Institute of Geology and Subsurface Research, Greece; Institut Français Pétrole. *Étude Géologique de l'Épire (Grèce Nord-Occidentale)*; Technip: Paris, France, 1966; p. 306.
33. Avdis, V.; Georgiou Ch Skourtsi-Koroneou, V.; Ioakeim, C.; Leontari, S. *Geological Map of Greece in Scale 1:50,000, "Agrinion" Sheet*; Institute of Geology and Mineral Exploration: Thens, Greece, 2013.
34. Karfakis, I.; Kanaki-Mauridou, F.; Tsaila-Monopoli, S. *Geological Map of Greece in Scale 1:50,000, "Alevrada" Sheet*; Institute of Geology and Mineral Exploration: Athens, Greece, 1989.
35. Smith, A.G. Othris, Pindos and Vourinos Ophiolites and the Pelagonian Zone. In Proceedings of the VI Colloquium Geology Aegean Region, Athens, Greece; 1977; pp. 1369–1374.
36. Robertson, A.H.F.; Clift, P.D.; Degnan, P.J.; Jones, G. Palaeogeographic and Palaeotectonic Evolution of the Eastern Mediterranean Neotethys. *Palaeogeogr. Palaeoclimatol. Palaeoecol.* **1991**, *87*, 289–343. [CrossRef]
37. Papanikolaou, D. Timing of Tectonic Emplacement of the Ophiolites and Terrane Paleogeography in the Hellenides. *Lithos* **2009**, *108*, 262–280. [CrossRef]
38. Ricci Lucchi, F. Depositional Cycles in the Two Turbidite Formations of Northern Apennines. *J. Sediment. Petrol.* **1975**, *45*, 3–43. [CrossRef]
39. Ricci Lucchi, F. The Foreland Basin System of the Northern Apennines and Related Clastic Wedges: A Preliminary Outline. *G. Geol.* **1986**, *48*, 165–185.

40. Vakalas, I. The Evolution of Foreland Basins in Western Greece. Ph.D. Thesis, University of Patras, Patras, Greece, 2003; p. 373.
41. Jacobshagen, V.; Richter, D.; Makris, J. Alpidic Development of the Peloponnesus. In *Alps, Apennines, Hellenides*; Closs, H., Roeder, D., Schmidt, H., Eds.; E. Schweizerbart'sche Verlagsbuchhandlung: Stuttgart, Germany, 1978; pp. 415–423.
42. de Graciansky, P.C.; Dardeau, G.; Lemoine, M.; Tricart, P. The Inverted Margin of the French Alps and Foreland Basin Inversion. In *Inversion Tectonics*; Cooper, M.A., Williams, G.D., Eds.; Geological Society, Special Publication: London, UK, 1989; Volume 44, pp. 87–104.
43. Doutsos, T.; Koukouvelas, I.K.; Xypolias, P. A New Orogenic Model for the External Hellenides. *Geol. Soc. Lond. Spec. Publ.* **2006**, *260*, 507–520. [CrossRef]
44. Weimer, P.; Pettingill, H.S. Deep-Water Exploration and Production: A Global Overview. In *Atlas of Deep-Water Outcrops*; AAPG Studies in Geology; American Association of Petroleum Geologists: Tulsa, OK, USA, 2007; Volume 56, pp. 12–16.
45. Piper, D.J.W.; Panagos, A.G.; Pe, G.G. Conglomeratic Miocene Flysch, Western Greece. *J. Sediment. Petrol.* **1978**, *48*, 117–126.
46. Pavlopoulos, A. Contribution to the Geological Investigation of Makrynoros Flysch Deposits, Akarnania. Ph.D. Thesis, Aristotle University of Thessaloniki, Thessaloniki, Greece, 1983.
47. Leigh, S.P. The Sedimentary Evolution of the Pindos Foreland Basin, Western Greece. Ph.D. Thesis, University of Wales, Cardiff, UK, 1991.
48. Leigh, S.P.; Hartley, A.J. Mega-Debris Flow Deposits from the Oligo-Miocene Pindos Foreland Basin, Western Mainland, Greece: Implications for Transport Mechanisms in Ancient Deep Marine Basins. *Sedimentology* **1992**, *39*, 1003–1012. [CrossRef]
49. Avramidis, P.; Zelilidis, A.; Vakalas, I.; Kontopoulos, N. Interactions between Tectonic Activity and Eustatic Sea-Level Changes in the Pindos and Mesohellenic Basins, NW Greece: Basin Evolution and Hydrocarbon Potential. *J. Petrol. Geol.* **2002**, *25*, 53–82. [CrossRef]
50. Konstantopoulos, P.A.; Zelilidis, A. Sedimentation of Submarine Fan Deposits in the Pindos Foreland Basin, from Late Eocene to Early Oligocene, West Peloponnesus Peninsula, SW Greece. *Geol. J.* **2013**, *48*, 335–362. [CrossRef]
51. British Petroleum Co. Ltd. (B.P.). *The Geological Results of Petroleum Exploration in Western Greece*; Institute for Geology and Subsurface Research: Athens, Greece, 1971; Special Report 10.
52. Fleury, J.J. Evolution d'une Plateforme et d'un Bassin dans Leur Cadre Alpin: Les Zones de Gavrovo-Tripolitze et du Pinde-Olonos. *Soc. Géol. Nord Spec. Publ.* **1980**, *4*, 651.
53. Wilpshaar, M. Applicability of Dinoflagellate Cyst Stratigraphy to the Analyses of Passive and Active Tectonic Settings. Ph.D. Thesis, University of Utrecht, Utrecht, The Netherlands, 1995.
54. Bellas, S.M. Calcareous Nannofossils of the Tertiary Flysch (Post-Eocene to Early Miocene) of the Ionian Zone in Epirus NW-Greece: Taxonomy and Biostratigraphical Correlations. In *Berliner Geowissenschaftliche Abhandlungen*; Selbstverlag Fachbereich Geowissenschaften: Berlin, Germany, 1997; Volume 22, p. 173.
55. Kaggle. Kaggle: Your Machine Learning and Data Science Community. Available online: https://www.kaggle.com (accessed on 19 January 2025).
56. Python Software Foundation. Python Programming Language, Version 3.10. Available online: https://www.python.org (accessed on 19 January 2025).
57. De Vries, B.; Huang, C.; Armston, J.; Huang, W.; Jones, J.W.; Lang, M.W. Rapid and robust monitoring of flood events using Sentinel-1 and Landsat data on the Google Earth Engine. *Remote Sens. Environ.* **2020**, *240*, 111664. [CrossRef]
58. Shekar, P.R.; Mathew, A. Morphometric Analysis of Watersheds: A Comprehensive Review of Data Sources, Quality, and Geospatial Techniques. *Watershed Ecol. Environ.* **2023**, *6*, 13–25. [CrossRef]
59. Evans, I.S. General geomorphometry, derivatives of altitude, and descriptive statistics. In *Spatial Analysis in Geomorphology*; Chorley, R.J., Ed.; Harper & Row: New York, NY, USA, 1972; pp. 17–90.
60. Singh, S.; Dubey, A. *Geoenvironmental Planning of Watersheds in Indian*; Chugh Publications: Allahabad, India, 1994; pp. 28–69.
61. Pike, R.J.; Wilson, S.E. Elevation relief ratio, hypsometric integral and geomorphic area altitude analysis. *Bull. Geol. Soc. Am.* **1971**, *82*, 1079–1084. [CrossRef]
62. ASF-ALOS PALSAR. ALOS PALSAR Overview. Available online: https://asf.alaska.edu/data-sets/sar-data-sets/alos-palsar/ (accessed on 10 December 2024).
63. Adiri, Z.; Lhissou, R.; Maacha, L.; Jilali, A.; Talbi, E.H.; Jellouli, A.; Chakouri, M. Comparison of ASTER GDEM3, SRTM3, NASADEM, TanDEM-X90, AW3D30, and ALOS PALSAR Data with TanDEM-X12: A Case Study of Tagragra of Akka Inlier, Moroccan Anti-Atlas. *Arab. J. Geosci.* **2022**, *15*, 1654. [CrossRef]
64. Mwaniki, M.W.; Moeller, M.S.; Schellmann, G. A Comparison of Landsat 8 (OLI) and Landsat 7 (ETM+) in Mapping Geology and Visualising Lineaments: A Case Study of Central Region Kenya. In Proceedings of the 36th International Symposium on Remote Sensing of Environment, Berlin, Germany, 11–15 May 2015. ISRSE36-61.
65. Qasim, M. Application of Remote Sensing for Geological Mapping Using Landsat Etm+ Satellite Image for part of Western Hazara Ranges Across Siran River, North Pakistan. *Pak. J. Hydrocarb. Res.* **2024**, *26*, 1–15.
66. Sabins, F.F. *Remote Sensing Principles and Interpretation*; W.H. Freeman Company: New York, NY, USA, 1997; pp. 366–371.

67. Khalifa, A.; Bashir, B.; Çakir, Z.; Kaya, Ş.; Alsalman, A.; Henaish, A. Paradigm of geological mapping of the adıyaman fault zone of eastern turkey using landsat 8 remotely sensed data coupled with PCA, ICA, and MNFA techniques. *Int. J. Geo-Inf.* **2021**, *10*, 368. [CrossRef]
68. Gasmi, A.; Gomez, C.; Zouari, H.; Masse, A.; Ducrot, D. PCA and SVM as geo-computational methods for geological mapping in the southern of Tunisia, using ASTER remote sensing data set. *Arab. J. Geosci.* **2016**, *9*, 753. [CrossRef]
69. Pour, A.B.; Hashim, M. Spectral Transformation of ASTER Data and the Discrimination of Hydrothermal Alteration Minerals in a Semi-Arid Region, SE Iran. *Int. J. Phys. Sci.* **2011**, *6*, 2037–2059.
70. Serbouti, I.; Raji, M.; Hakdaoui, M.; El Kamel, F.; Pradhan, B.; Gite, S.; Alamri, A.; Maulud, K.N.A.; Dikshit, A. Improved Lithological Map of Large Complex Semi-Arid Regions Using Spectral and Textural Datasets within Google Earth Engine and Fused Machine Learning Multi-Classifiers. *Remote Sens.* **2022**, *14*, 5498. [CrossRef]
71. Nielsen, A.A. Kernel maximum autocorrelation factor and minimum noise fraction transformations. *IEEE Trans. Image Process.* **2011**, *20*, 612–624. [CrossRef] [PubMed]
72. Tatar, A.; Haghighi, M.; Zeinijahromi, A. Experiments on Image Data Augmentation Techniques for Geological Rock Type Classification with Convolutional Neural Networks. *J. Rock Mech. Geotech. Eng.* **2024**, *17*, 106–125. [CrossRef]
73. Ghaznavi, A.; Saberioon, M.; Brom, J.; Itzerott, S. Comparative Performance Analysis of Simple U-Net, Residual Attention U-Net, and VGG16-U-Net for Inventory Inland Water Bodies. *Appl. Comput. Geosci.* **2024**, *21*, 100150. [CrossRef]
74. Massironi, M.; Bertoldi, L.; Calafa, P.; Visonà, D.; Bistacchi, A.; Giardino, C.; Schiavo, A. Interpretation and Processing of ASTER Data for Geological Mapping and Granitoid Detection in the Saghro Massif (Eastern Anti-Atlas, Morocco). *Geosphere* **2008**, *4*, 736–759. [CrossRef]
75. Dang, K.B.; Nguyen, M.H.; Nguyen, D.A.; Phan, T.T.H.; Giang, T.L.; Pham, H.H.; Nguyen, T.N.; Tran, T.T.V.; Bui, D.T. Coastal Wetland Classification with Deep U-Net Convolutional Networks and Sentinel-2 Imagery: A Case Study at the Tien Yen Estuary of Vietnam. *Remote Sens.* **2020**, *12*, 3270. [CrossRef]
76. Chen, P.; Su, X.; Liu, M.; Zhu, W. Lensless Computational Imaging Technology Using Deep Convolutional Network. *Sensors* **2020**, *20*, 2661. [CrossRef]
77. Huang, G.; Liu, Z.; Van Der Maaten, L.; Weinberger, K.Q. Densely Connected Convolutional Networks. In Proceedings of the 2017 IEEE Conference on Computer Vision and Pattern Recognition (CVPR), Honolulu, HI, USA, 21–26 July 2017; pp. 2261–2269.
78. Zhang, K.; Zuo, W.; Chen, Y.; Meng, D.; Zhang, L. Beyond a Gaussian Denoiser: Residual Learning of Deep CNN for Image Denoising. *IEEE Trans. Image Process.* **2017**, *26*, 3142–3155. [CrossRef]
79. Qi, W.; Wei, M.; Yang, W.; Xu, C.; Ma, C. Automatic Mapping of Landslides by the ResU-Net. *Remote Sens.* **2020**, *12*, 2487. [CrossRef]
80. Oktay, O.; Schlemper, J.; Le Folgoc, L.; Lee, M.; Heinrich, M.; Misawa, K.; Mori, K.; McDonagh, S.; Hammerla, N.Y.; Kainz, B.; et al. Attention U-Net: Learning Where to Look for the Pancreas. *arXiv* **2018**, arXiv:1804.03999. [CrossRef]
81. Abdullah, M.A.M.; Mohammed, A.A.; Awad, S.R. RockDNet: Deep Learning Approach for Lithology Classification. *Appl. Sci.* **2024**, *14*, 5511. [CrossRef]
82. Bahrami, H.; Esmaeili, P.; Homayouni, S.; Pour, A.B.; Chokmani, K.; Bahroudi, A. Machine Learning-Based Lithological Mapping from ASTER Remote-Sensing Imagery. *Minerals* **2024**, *14*, 202. [CrossRef]
83. Long, J.; Shelhamer, E.; Darrell, T. Fully Convolutional Networks for Semantic Segmentation. In Proceedings of the IEEE Conference on Computer Vision and Pattern Recognition, Boston, MA, USA, 7–12 June 2015; pp. 3431–3440. [CrossRef]
84. Rahman, M.A.; Wang, Y. Optimizing intersection-over-union in deep neural networks for image segmentation. In Proceedings of the International Symposium on Visual Computing, Las Vegas, NV, USA, 12–14 December 2006; Springer: Cham, Switzerland; Berlin/Heidelberg, Germany, 2016; pp. 234–244.
85. Han, W.; Zhang, X.; Wang, Y.; Wang, L.; Huang, X.; Li, J.; Wang, S.; Chen, W.; Li, X.; Feng, R.; et al. A Survey of Machine Learning and Deep Learning in Remote Sensing of Geological Environment: Challenges, Advances, and Opportunities. *ISPRS J. Photogramm. Remote Sens.* **2023**, *202*, 87–113. [CrossRef]
86. Sun, W.; Zhou, J.; Meng, X.; Yang, G.; Ren, K.; Peng, J. Coupled Temporal Variation Information Estimation and Resolution Enhancement for Remote Sensing Spatial–Temporal–Spectral Fusion. *IEEE Trans. Geosci. Remote Sens.* **2023**, *61*, 5532118. [CrossRef]
87. Blaschke, T.; Kelly, M.; Merschdorf, H. Object-based image analysis: Evolution, history, state of the art, and future vision. In *Remotely Sensed Data Characterization, Classifcation, and Accuracies*; Thenkabail, P.S., Ed.; UC: Berkeley, CA, USA, 2015.
88. Pandey, P.C.; Koutsias, N.; Petropoulos, G.P.; Srivastava, P.K.; Dor, E.B. Land use/land cover in view of earth observation: Data sources, input dimensions, and classifers–a review of the state of the art. *Geocarto Int.* **2021**, *36*, 957–988. [CrossRef]
89. Ma, X.; Wang, H.; Wang, J. Semisupervised classification for hyperspectral image based on multi-decision labeling and deep feature learning. *ISPRS J. Photogramm. Remote Sens.* **2016**, *120*, 99–107. [CrossRef]
90. Ma, L.; Liu, Y.; Zhang, X.; Ye, Y.; Yin, G.; Johnson, B.A. Deep learning in remote sensing applications: A meta-analysis and review. *ISPRS J. Photogramm. Remote Sens.* **2019**, *152*, 166–177. [CrossRef]

91. Giang, T.L.; Dang, K.B.; Le, Q.T.; Nguyen, V.G.; Tong, S.S.; Pham, V.-M. U-Net Convolutional Networks for Mining Land Cover Classification Based on High-Resolution UAV Imagery. *IEEE Access* **2020**, *8*, 186257–186273. [CrossRef]
92. Diakogiannis, F.I.; Waldner, F.; Caccetta, P.; Wu, C. ResUNet–A: A Deep Learning Framework for Semantic Segmentation of Remotely Sensed Data. *ISPRS J. Photogramm. Remote Sens.* **2020**, *162*, 94–114. [CrossRef]

Disclaimer/Publisher's Note: The statements, opinions and data contained in all publications are solely those of the individual author(s) and contributor(s) and not of MDPI and/or the editor(s). MDPI and/or the editor(s) disclaim responsibility for any injury to people or property resulting from any ideas, methods, instructions or products referred to in the content.